POLITECNICO
MILANO 1863

SCUOLA DI INGEGNERIA INDUSTRIALE
E DELL'INFORMAZIONE

# Analysis and Optimization of a Scintillator Calorimeter System for Pulsed Radiation Spectrometry at ELI Beamlines

Tesi di Laurea Magistrale in
Nuclear Engineering - Ingegneria Nucleare

**Lorenzo Sostero, 967206**

**Advisor:**
Prof. Marco Caresana

**Co-advisor:**
Ph.D. Benoit Lefebvre

**Academic year:**
2021-2022

**Abstract:** During the generation of a laser-induced particle beam, a non-negligible fraction of the laser energy is dissipated in the form of ionizing radiation, whose characteristics strongly depend on the underlying physics of the laser-plasma. The peculiar pulsed time structure of these radiation fields prevents the use of conventional instruments used for nuclear spectroscopy, as they operate with a very long readout dead time compared to the time evolution of the pulse. In this context, the OSCAR detector has been developed: an innovative online scintillation detector that can be used for characterizing the radiation produced in high intensity laser-target experiments. After an introduction to the working principle of the detector and its design, an in-depth analysis and optimization of the crystal light output and collection are reported. The use of $TiO_2$ painting as reflector layer around scintillating crystals has been explored. The background noise variations in time and the point of view effects related to the actual CMOS camera based readout system have been investigated in detail. The analysis underlined the limitations of the system, and silicon photodiodes have been presented as alternative light sensors to CMOS camera. Simulations of the propagation of optical photons from the scintillation medium to the CMOS sensor have been performed with FLUKA.CERN Monte Carlo code. Novel optical models have been developed for simulating reflections of optical photons on non-smooth surfaces. The observed deviations of the simulated light output distribution in space with respect to experimental data are comparable to the experimental error. An estimation of the time straggling due to photon propagation inside the crystal has been also performed. Finally, OSCAR's neutron detection capabilities have been investigated. The estimated low neutron sensitivity indicates that further development in design and readout techniques are necessary to achieve direct neutron detection with OSCAR, and possible improvements are proposed.

**Key-words:** Detector modelling and simulations, nuclear instruments and methods for plasma diagnostic, optical simulations, readout detector system.

## 1. Introduction

The ELI Beamlines Facility in Dolní Břežany (Czech Republic) is a leading laser research center and part of ELI (Extreme Light Infrastructure) pan-European Research Infrastructure hosting some of the world most intense

lasers, as the L3 laser system called HAPLS (The High-Repetition-Rate Advanced Petawatt Laser System) that is designed to deliver PW pulses with energy of at least 30 J, and durations $< 30$ fs, and the L4 laser system called ATON, which is designed to generate pulses of 10 PW with duration of 150 fs [1]. ELI Beamlines aims to provide laser-generated radiation beams for multidisciplinary user research [2]: not only for research in physics and material science, but also in life science, laboratory astrophysics, and chemistry [1]. The laser beams are sent to various experimental rooms. Depending on the experimental setup, a wide range of possible radiation fields and particles beams are produced as a result of laser interactions [2].
The interaction of these high intensity lasers with matter induces ionization of the target material, that leads to the formation of a plasma and so the emission of a considerable amount of charged particles and photons [3–5]. Typically, a population of relativistic electrons is formed in the laser-generated plasma, the so-called "hot electrons" [6, 7], which travels in the plasma under the action of electromagnetic forces. The motion of this hot electron beam through the target requires the presence of a return current, that is provided by a second electron species, the so-called "cold electrons", whose temperature is much lower than that of the hot electrons (tens of keV for cold electrons against MeV of hot electrons) [8]. Hot/cold electrons produce respectively hot/cold photons via Bremsstrahlung processes in the target, and the energy spectrum of this radiation is again well described by a Maxwell-Boltzmann distribution [5]. Photon emission could be exploited in the analysis of the interaction [5], as well as in several medical and industrial applications, as for radiography of dense objects [9] and cancer radiotherapy [10].
In addition to Bremsstrahlung photons, high energy pulsed beams of electrons, protons and ions can be emitted as a consequence of the laser-target interaction [11, 12]; this is at the basis of the laser-driven acceleration of particles. The interest around this technology is related to the numerous innovative applications in scientific research (nuclear physics, high energy-density physics, inertial fusion), as well as in technology (material engineering) and medicine (hadron cancer therapy, production of isotopes for PET) [13].

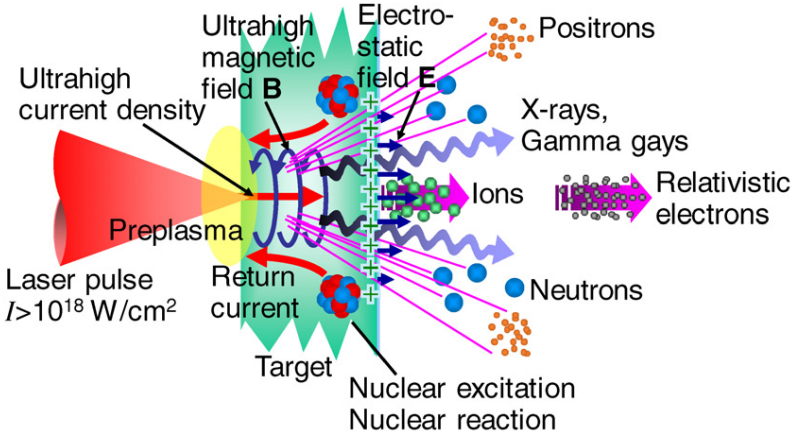


Figure 1: Sketch of an ultra-high intensity laser interaction with a target [14].

The large amount of radiation produced in laser-target experiments is strongly related to the plasma temperature and transport phenomena. Therefore, it also offers a valuable source of information on the laser-matter interaction. For this reason, an online analysis of the produced radiation field also represents a useful diagnostic tool for the plasma produced [15].
Laser-induced radiation fields are extremely short-lived, of the order of the laser pulse, that is a few femtoseconds [2]. Typical spectrometry techniques in radiation detection rely on single-quanta measurement: once the radiation interact with the detector, there is a dead time in which the instrument is blind to the incoming radiation. Therefore, in the case of a burst of radiation, a conventional online detector would be subjected to pile-up that makes the reading of the instrument meaningless [16]. Viable solutions for pulsed radiation fields detection are offered by passive detectors, as thermoluminescence dosimeters (TLD) and optically stimulate luminescence dosimeters (OSL), and also by online specialized detectors as the LB 6419 "Pandora detector" [17] and the "LUPIN detector" [18]. However, these detectors do not allow performing a spectrometry of the radiation produced in the plasma interaction, and so the OSCAR detector (Online Scintillator Calorimeter for the Analysis of Radiation) has been developed from the Radiation Protection Group at ELI Beamlines to perform shot-by-shot energy spectrum measurements in high intensity and pulsed fields typically produced in laser-target interactions.
The OSCAR design was inspired by other segmented electromagnetic calorimeters used in the field of high energy physics, which are a set of scintillating layers measuring the energy deposited at different depths in the material [2]. Similarly, the OSCAR detector is composed by a stack of scintillator crystals that emit visible light as a consequence of the interaction with ionizing radiation [16]. A CMOS camera collects the light from

the crystals, and from the intensity of the luminous signal it is possible to evaluate the Maxwell-Boltzmann temperature of the radiation interacting with the detector.

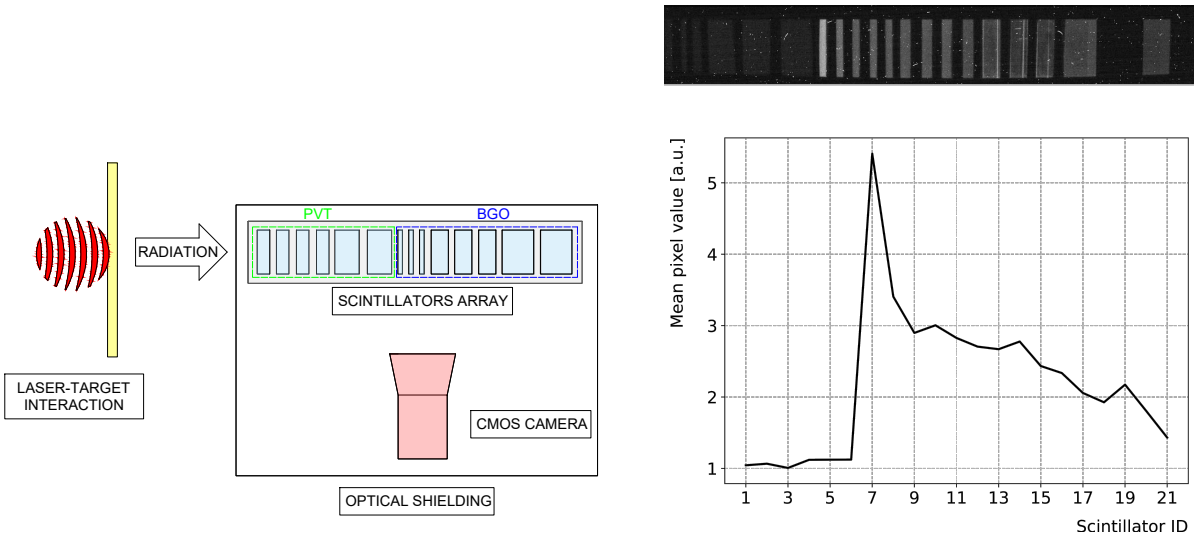


(a) (b)

Figure 2: The OSCAR detector working principle. Schematic of experimental setup (a) and example of a picture acquired after a shot at ELIMAIA and post-processed shot data (b).

The OSCAR detector is currently installed inside the interaction chamber at the ELIMAIA beamline, where it is used as a diagnostic tool with the purpose of measuring the temperature of the plasma produced. ELIMAIA is one of the experimental rooms at ELI Beamlines, and it consists of two main subsystems: the ion accelerator – that is the interaction chamber in Figure 3 – and the ELI MEDical applications (ELIMED) beam transport and dosimetry section [19]. At ELIMED, very high-dose-rate (around Gy/min) controlled proton and ion beams, with energy levels ranging from 5 to 250 MeV, are transported to an in-air section dedicated to absolute and relative dosimetry of the laser-generated ions. The ELIMED beamline, indeed, was designed and realized with the long-term goal of exploring medical applications and to obtain extremely high shot-to-shot reproducibility, high precision in the delivered dose, quasi-monoenergetic beam spectra at the biological sample, and reproducibility of the transported beams [20]. ELIMAIA is primarily served by the L3 laser system, and the laser beam is typically focused on a solid target for the purpose of ion acceleration [2].

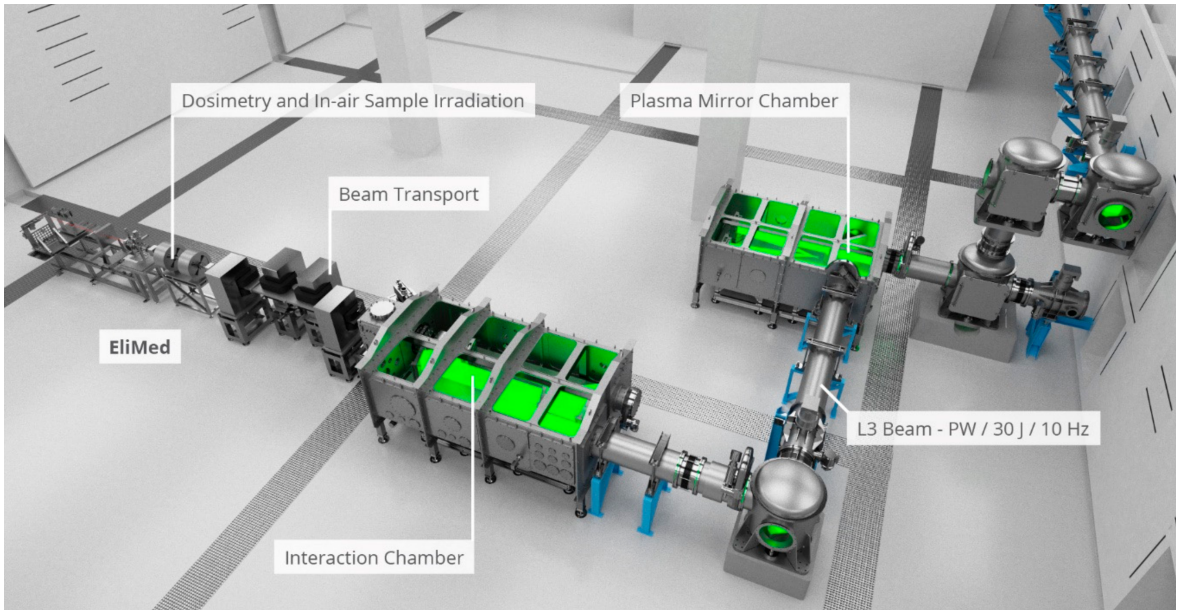


Figure 3: Rendering of the ELIMAIA experiment [19].

In the following section, the OSCAR's design principle is explained more in the details, and the use of a new reflecting material around the crystal is explored to optimize the light output from the crystal. The readout

system that collects the light signal from the scintillator is analyzed in Section 3, and in particular the current camera-based technique is described in Section 3.1. A new readout system based on the use of silicon photodiodes is proposed in Section 3.2. In Section 4, three optical models are introduced (Sections 4.2, 4.3, 4.4) and applied to simulate optical photon propagation in the crystal using the FLUKA.CERN code. Models are benchmarked on experimental data (Section 4.5), and also employed to predict the time straggling of photons due to their propagation inside the crystal (Section 4.6). Finally, in Section 5 OSCAR's neutron capabilities are explored, and some improvements on the detector for neutron detection are proposed.

## 2. Design and Light Output Optimization of OSCAR

The OSCAR detector is specifically designed for measuring the energy of intense pulsed radiation fields produced in high intensity laser-target experiments [15]. It is composed by a stack of scintillating crystals, as shown in Figure 2a, which emit visible light when interacting with radiation. The actual design of the detector is tuned for X-ray and electron detection in the MeV range, but the same working principle could also be employed also for other applications, as for proton detection [5].
The scintillation light is captured by a CMOS camera, triggered by the laser clock itself, allowing an online data acquisition. The stack of scintillators and the CMOS camera are installed inside a compact plastic light-tight box, to shield the CMOS camera from the ambient optical light. As shown in Figure 2b, the camera records greyscale images with 8-bit or 16-bit format that are saved in the TIFF or BMP format on a disk (for the experimental campaigns in this work, 8-bit format images were used). The light output intensity from each crystal is taken as the mean pixel value (MPV) calculated on a predefined region-of-interest (ROI) inside the crystal area, with background subtraction. From the relative variation of the MPVs among the various crystals, it is possible to estimate, through an unfolding procedure, the energy of the radiation detected.

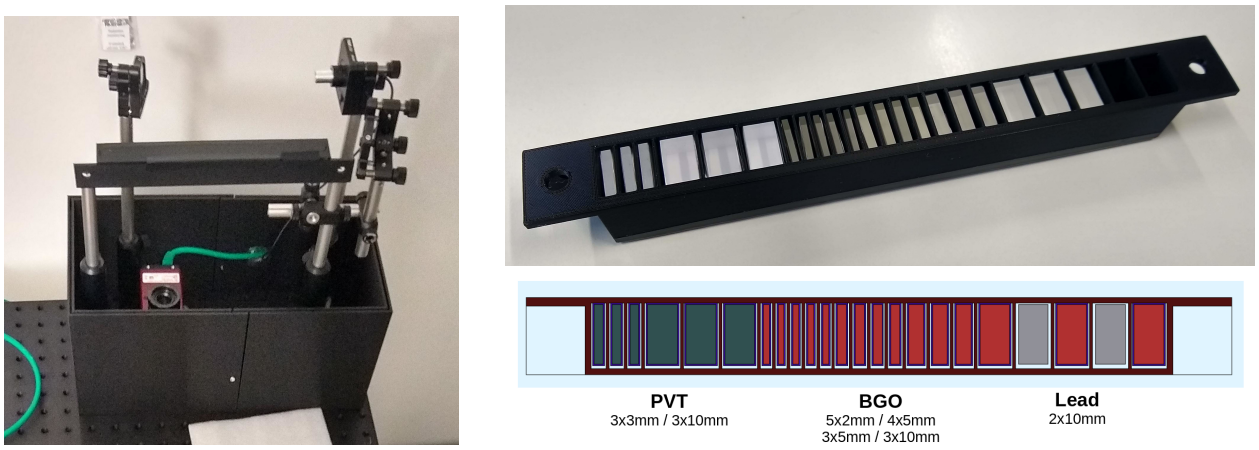


Figure 4: OSCAR detector with opened dark box to show the relative positioning of the camera and scintillator stack.

A more precise scheme of the design of the stack of scintillators is presented in Figure 4, where several elements are identified inside the black crystal holder:

- polyvinyltoluene-based (EJ-200 [21]) crystals with low-photon cross-section for electron absorption;
- bismuth germanium oxide (BGO) crystals with high-density for photon absorption;
- lead filters to improve photon absorption.

As shown in Figure 5, the laser-induced radiation impinge the plastic scintillator first. The following region encountered by the radiation that has not interacted with EJ-200 is therefore the one with BGO crystals, that has a much higher density and so a higher capability of interaction with radiation [5], see also Table 1. The scintillation light decay times for EJ-200 and BGO are 2.1 ns and 300 ns, respectively, and the exposure time of the camera is set much larger than these characteristic times. The entire system crystals-camera can achieve the maximum repetition rate of 50 Hz, which is well beyond the capabilities of preset and near-future laser systems [5].
All the crystals have a cross-section of 2x2 $cm^2$, and their thickness typically increases as the radiation penetrates in the detector: this helps in capturing the beginning of the dose-depth curve in high detail, ensuring better energy resolution at the peak region, while limiting the noise in the second part [5, 15], as shown in Figure 5. However, the design can be easily adapted for the needs of an experiment, simply changing the crystals holder and using the readily available crystals.

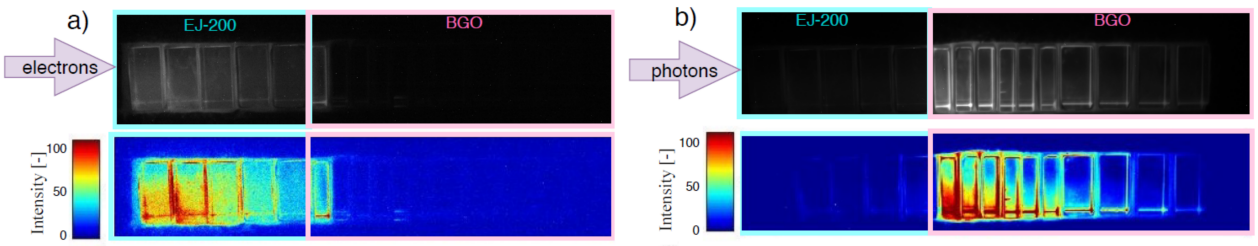


Figure 5: Comparison between the detector response (previous prototype) when it is exposed to accelerated electrons (a) and to the secondary Bremsstrahlung photons (b). The top figures show the raw signal from the camera and the bottom ones the post-processed signal [5]

| Material | Density [g/cm$^3$] | Light Yield [photons/MeV] | Wavelength of max Emission [nm] | Decay Time [ns] | Refraction Index |
|---|---|---|---|---|---|
| EJ-200 | 1.03 | 10'000 | 425 | 2.1 | 1.58 |
| BGO | 7.13 | 8'200 | 480 | 300 | 2.15 |

Table 1: Main parameters of scintillating materials chosen for the current setup of OSCAR [16].

In addition to measuring the intensity of the incoming radiation, the OSCAR detector estimates the temperature of the Maxwellian-Boltzmann energy distribution of hot electrons ($T_{e,\mathrm{h}}$), hot photons ($T_{\gamma,\mathrm{h}}$) and cold photons ($T_{\gamma,\mathrm{c}}$) produced in the laser-plasma interaction (the signal from cold electrons is assumed to be negligible, since their range is typically smaller than the thickness of the viewport). To translate the light output from the crystal into these temperatures, an unfolding procedure is needed. The measured light output intensity from each crystal $L_i$ is fitted to the unfolding model to obtain best-fit amplitudes $A$ and temperatures $T$:

$$L_i = A_{e,h} M_i^e(T_{e,h}) + A_{\gamma,c} M_i^\gamma(T_{\gamma,c}) + A_{\gamma,h} M_i^\gamma(T_{\gamma,h})$$

The response matrixes $M^e$ and $M^\gamma$ employed in the unfolding algorithm are obtained through Monte Carlo simulations using FLUKA.CERN code, where it is estimated the energy deposited in each crystal in function of the type and the temperature of the incident radiation, assuming a Maxwellian-Boltzmann energy distribution. From energy deposition simulations, it is possible to assess the corresponding light output using experimental calibration coefficients, assuming that the scintillator response doesn't depend on the type of the incident radiation (since in any case secondary electrons are the particles exciting energy levels in the crystal [16]), and that the light output is linear with the energy deposition (that means no saturation effects due to the high intensity of the impinging radiation [22]).
A pictorial representation of the response matrixes for electrons and photons in function of the temperature of the impinging radiation is shown in Figure 6. Higher responses to electrons are apparent on the first crystals of EJ-200, while the very first BGO crystals are the ones most sensible to photons.

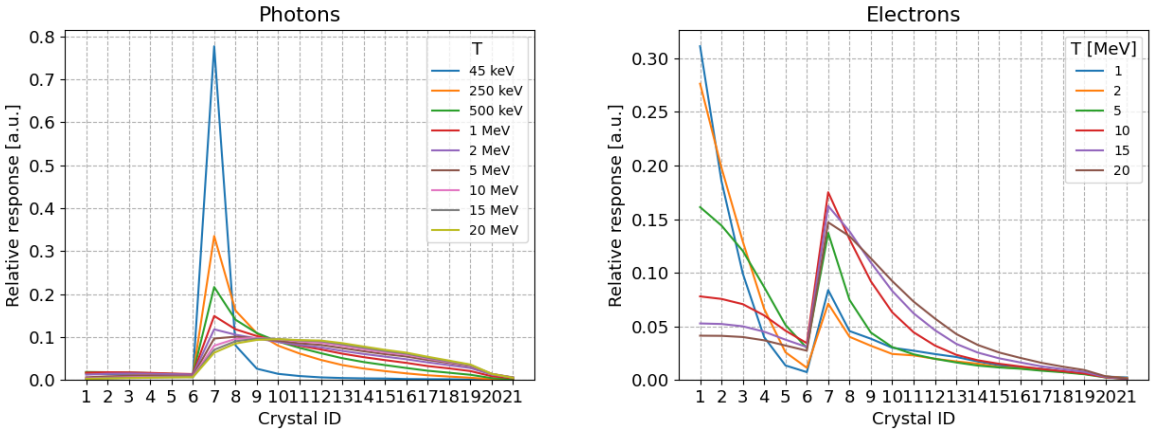


Figure 6: Graphical representation of the response matrix for electrons and photons in function of different temperatures.

Monte Carlo codes have been widely recognized as suitable tools for studying the motion and interaction of particles – intended in a very broad sense, from hadrons to leptons and photons. Citing J. Hendricks [23], Monte Carlo methods "are based on calculating the average or probable behavior of a system by observing the outcomes of a large number of trials at a game of chance that simulates the physical events responsible for the behavior". Among the most successful Monte Carlo codes in nuclear physics, the FLUKA.CERN code [24–26] can be used for simulating the interaction and transport of hadrons, heavy ions, and electromagnetic particles from few keV (or thermal energies for neutrons) to cosmic ray energies in arbitrary materials [25].
The energy-light calibration was performed using a setup as the one shown in Figure 7, where the crystal is placed in between the CMOS camera and a Cs-137 source, that emits isotopically $\gamma$-ray photons with energy 661.7 keV. The camera and the crystal holder were mounted in a light-tight box, to reduce as much as possible the environmental optical light contamination. The measured MPV was compared to the simulated crystal response estimated through FLUKA.CERN simulations, and so the calibration coefficients were assessed.

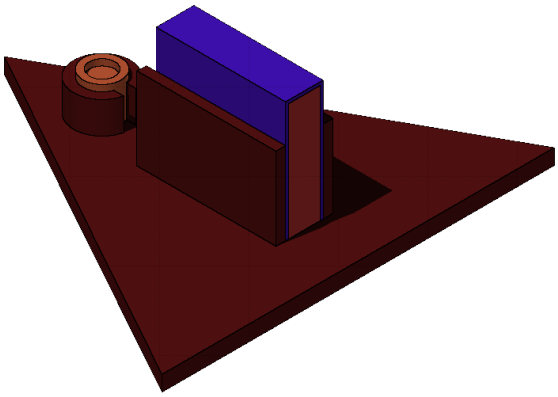

Figure 7: 3D view of the geometry model for the plastic holder supporting the crystal and the Cs-137 source.

At this point, it should be clear that the light signal emitted from the crystal should be intense enough to have a reliable estimation of the temperatures of the radiation field with low uncertainties. For this reason, all the faces of the scintillation crystals in OSCAR (except the one in front of the readout system) are covered with a polytetrafluoroethylene (PTFE) tape, a highly reflective material [27], to enhance the fraction of light produced in the crystal reaching the optical photon detector. A dedicated experimental study of the dependence of the mean pixel value in function of the thickness of the PTFE wrapping was already performed. The results indicated that the light output can be significantly enhanced using a PTFE reflector, but it has been also observed that for few PTFE layers a small imprecision in the wrapping process could lead to a substantial difference in crystal responses. To solve the problem, it was concluded that at least four layers of PTFE tape (approximately 0.5 mm of PTFE) should be used for scintillator wrapping [15].
In more recent studies, it has been observed that the light output from the same crystal with four different wrappings (but always four layers of PTFE), applied by the same operator, shows a deviation of $> 5\%$, that is unacceptable for our purposes, since this would require to perform a calibration for every wrapped crystal, which is impractical. It is important to remark that non-uniformity of the light output for each given crystal material and thickness has a direct impact on the accuracy of the unfolding procedure, which uses the relative light output of crystals in the stack. The quality of the reflector could mitigate the systematic uncertainty associated to variations in the reflector effectiveness, therefore it could be interesting to explore the titanium oxide ($TiO_2$) painting as an alternative reflector to PTFE wrapping.
This type of reflector is widely used for scintillator detectors, since it is a diffusive reflector with good reflective properties, even though reflectivity is not as good as PTFE [27]. However, the $TiO_2$ offers interesting properties for our purposes: in fact, it is available as liquid paint to spray on the crystal faces, therefore it is possible to apply the reflector layer with a more standardized method and more uniformly with respect to PTFE wrapping, reducing, for example, the possibility of having non-uniformities due to air bubbles in between reflector and crystal. Eventually, the $TiO_2$ layer is more likely to be subjected to cracks and dis-homogeneities on the thickness of the painting rather than air bubbles, but it is possible to spot these kind defects on the painting (and successively correct them) simply by illuminating the naked face with a strong light, as shown in Figure 8. Finally, the PTFE wrapping can be accidentally altered in mounting the crystal on its holder, while the painting remains fixed to the crystal (but still cleaning operation of the naked face deserves particular attention, since some painting could be scratched from borders).

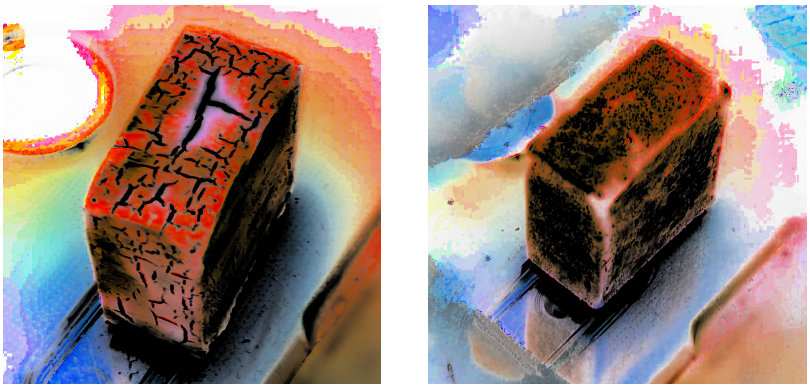

(a) (b)

Figure 8: Color inverted pictures of the same BGO crystal with two different $TiO_2$ paintings applied. Painting with a severe crack on the top of the crystal and smaller ones all around (a), and uniform painting with finely diffused small bubbles (b).

Analogously to the analysis performed on the PTFE wrapping [15], it was found that the maximum reflectivity and uniformity of the painting are achieved after five layers of $TiO_2$. In addition, it has been measured a value of light output from a BGO crystal with five layers of $TiO_2$ coating 7.21% lower than from the same crystal with four layers of PTFE (see Figure 9), that is consistent with what reported in literature [27].

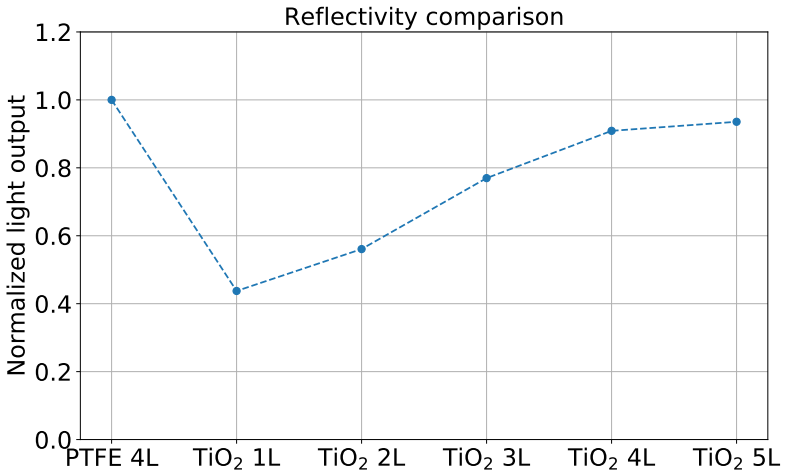


Figure 9: Light output comparison in between four layers of PTFE reflector and different number of layers of $TiO_2$ reflector.

The assessment of the absolute value of the reflectivity index of the painting is instead a more complex subject, but it can be issued comparing experimental measurements and optical simulations, where the reflectivity of the PTFE layer is left as fitting parameter. This is performed in the Section 4.5, where the point of view effects (see Section 3.1.2) have been exploited to retrieve the reflectivity of the PTFE layer.
As a final remark, it should be noticed that also the surface roughness of crystal plays a role in light reflection and distribution. The actual design has the face exposed to the camera polished, and the other five faces of the crystal mechanically etched, which is useful to solve the problem of "corner effect" previously observed [15]. However, also other type of surface treatments are known for their effectiveness [28], and in the future other surface treatments will be explored.

## 3. Readout System of OSCAR

The scintillation light is used to estimate the energy deposition in each crystal. One possibility, that is the one currently adopted in OSCAR, is using a CMOS camera to take a picture of the entire stack of scintillating

crystals. The camera acquires the light signal over an exposure time, integrating the light emitted towards the lens of the camera. From the picture, it is possible to obtain a useful measure of the light output from each crystal, that is the mean pixel value (MPV) calculated on a certain region-of-interest (ROI) inside the crystal area. In this procedure, it is assumed that the MPV only depends on the crystal where the ROI is defined, and not on the neighboring scintillators, hence cross-talk effects are neglected. The CMOS camera system is analyzed more in the details in Section 3.1.
As an alternative light sensor to CMOS camera, silicon photodiodes (SiPD) are investigated in Section 3.2. The SiPD directly converts the optical light output from the crystal in electric signal, that has to be handled by a dedicated amplification circuit before arriving to the digitizer.

## 3.1. CMOS Camera Readout

The CMOS camera used in the current readout system is provided by Allied Vision, and the model is Manta G-235. The MPV evaluated from the picture over a certain ROI needs to be subtracted by the background, and this requires a precise knowledge of the background of the camera itself. However, it was noticed that the background fluctuates quite significantly in time, and this aspect deserved a further investigation, that is reported in Section 3.1.1.
The light captured by the camera also depends on the position of the light sensor with respect to the crystal, and this point of view effect is described in Section 3.1.2.

### 3.1.1 Background Analysis

Pictures taken from the CMOS camera cannot be considered as background-free, since pixels are fired also by the external light penetrating inside the OSCAR box. Also, the noise of the camera itself induces some level of background on pixel values, that has to be subtracted from the MPV associated to the signal.
There are several components of noise for a camera [29]:

- Dark shot noise: dark current is a current that flows even when no photons are incident on the camera. It is a quantum phenomenon resulting from electrons spontaneously generated within the silicon chip (valence electrons are thermally excited into the conduction band). The variation in the amount of dark electrons collected during the exposure is the dark shot noise. It is independent of the signal level, but it is dependent on the temperature of the sensor.
- Read noise: this is the noise generated in processing the electronic signal. This depends on the sensor design and on the camera electronics.
- Photon shot noise: this is the statistical noise associated to the number of photons arriving at the pixel within the exposure time, whose variations are described by Poisson statistics. The photon shot noise is independent of sensor temperature.
- Fixed pattern noise: this is caused by non-uniformities of the pixel size, and it is independent of signal level and temperature of the sensor.

As a consequence of the background, pictures will appear as a "starry sky", where pixel values are not uniformly equal to 0, although there are no light sources facing the camera. Furthermore, some pixels are saturated (the so-called "hot pixels" or "dead pixels"), and must be removed before estimating the MPV of the signal.
For the specific camera used in OSCAR, it was observed that the background significantly changes in time. In Figure 10, it is shown the MPV measured on a long time range – 28 hours from the switching on from cold conditions – with the camera inside a light-tight box with no internal light sources. In the first two hours from the switching on, the background progressively increases due to the heating up of the system. Then, a saturation level is reached, and peaks from the saturation level are explained by the camera image processing, that heats up the camera and increase thermal noise.
To reduce the background, it could be worth it to substitute the camera with a cooled one (Peltier camera). As a good practice, the camera should not be used in free-running mode, but it should be switched on shortly before the picture acquisition, on the contrary of the free-running mode where the acquisition is in continuous. This is what is already done at ELIMAIA, where the camera system is synchronized with the laser pulse impinging on the target.
In addition to the interest toward the background fluctuations in time, there was the needing to better investigate which is the proper ROI to take when evaluating the mean pixel value related to the background. Two options are foreseen:

- selecting a large portion of the picture outside the crystal ROIs;
- selecting the ROIs of the crystals.

The mean pixel value in the two regions should be the same in both cases if the background is uniformly distributed. However, it was observed that all around the border of the picture the background is much higher.

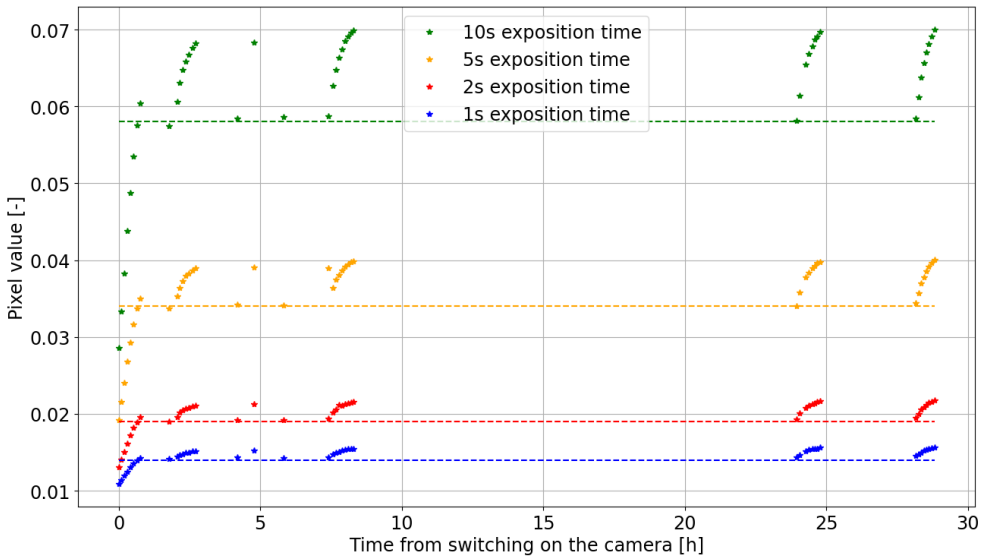


Figure 10: Background analysis in time for 1s, 2s, 5s and 10s of exposition time of the CMOS camera.

For this reason, the background should be assessed on a ROI in correspondence to the crystal, even though this leads to evaluate a lower number of pixels, and so to a higher uncertainty on the MPV.

### 3.1.2 Point of View Effect Analysis

The amount of light collected by the camera lens depends on the position of the camera with respect to the face of the crystal. This effect is called the "point of view" effect (POV effect). It's an important systematic effect that must be corrected during the analysis of OSCAR data, and in principle it could be exploited to develop advanced optical models in FLUKA, which would be useful in the optimization of the detector and in understanding the effects of optical parameters on the light output. In fact, in principle the POV effect depends on various characteristics of the crystal setup, as the roughness of surfaces, the reflectivity coefficient of the reflector, the type of reflector and the coupling between reflector and crystals, to name a few.
As a first step in the study of the POV effect, a simple empirical model is developed assuming the crystal as an isotropic source of light. The light coming from the crystal will be refracted at the interface crystal-air following Snell's law:

$$n\ \sin(\theta_i) = \sin(\theta_o),$$

where $\theta_i$ and $\theta_o$ are the incoming and outcoming angles with respect to the normal of the crystal-air interface, and $n$ is the index of refraction of the crystal. The index of refraction of air is assumed to be unitary. Supposing that light propagates isotropically inside the crystal, the probability density function (p.d.f) for $\theta_i$ is a step function whereby:

$$f(\theta_i) = \begin{cases} 1 & \text{if } 0 \leq \theta_i \leq \pi/2 \\ 0 & \text{otherwise} \end{cases}.$$

At this point, the p.d.f. for $\theta_o$ can be obtained through a change of random variable using the expression:

$$f_Y(y) = f_X(g^{-1}(y)) \left| \frac{d}{dy}(g^{-1}(y)) \right|, \tag{1}$$

where $f_Y(y)$ is the p.d.f. of a function $g(x)$ provided that $x$ is a random variable with a p.d.f. $f_X(x)$, and $g^{-1}$ is the inverse of the $g$-function. For this specific problem:

$$\begin{gathered} f_X \rightarrow f_{\theta_i} \\ f_Y \rightarrow f_{\theta_o} \\ g(x) = \arcsin(n\ \sin(\theta_i)). \end{gathered}$$

In practice, the first term of Eq. (1) is either 1 or 0, and therefore it has the only effect to restrict the domain of $f(\theta_o)$. Since $0 \leq \theta_o \leq \pi/2$, the allowed values for $\theta_i$ are in the range between $[g^{-1}(0); g^{-1}(\pi/2)]$, and the

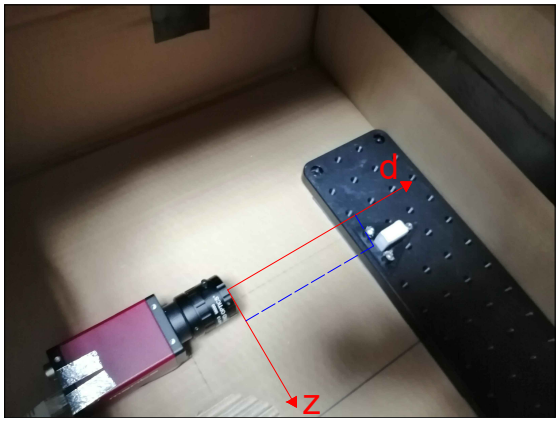


(a)

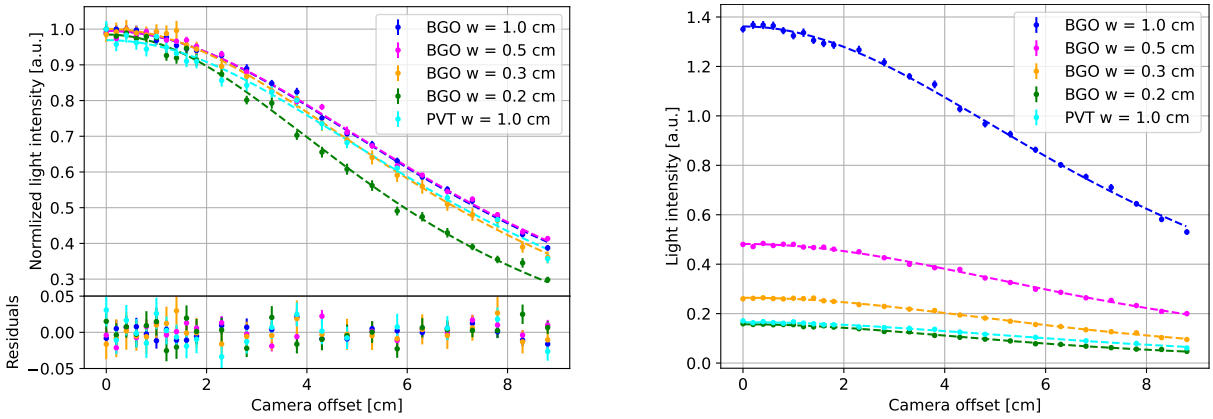


(b)

Figure 11: Experimental setup (a) and results (b) of the POV effect analysis, fitted with the empirical model in Eq. 2.

upper bound is $\leq \pi/2$, since $n \geq 1$, and so the first term is always equal to 1. The p.d.f. for the outcoming angle goes as:

$$f_{\theta_o}(\theta_o) \propto \frac{\cos(\theta_o)}{\sqrt{1 - \frac{\sin^2(\theta_o)}{n^2}}}.$$

The light ray therefore exits the crystal with an angle $\theta_o$, and hits a plane parallel to the crystal at a distance $d$ in the position $z = d\ \tan(\theta_o)$ (see also Figure 11a). In other words, $z$ is the distance in between the crystal axis and the camera lens axis, that is exactly the variable of interest in the experimental measure of the POV effect. Again, the p.d.f of $z$ can be obtained through a change of variable:

$$f_Z(z) \propto \frac{1}{(d^2 + z^2)^{\frac{3}{2}}} \frac{1}{\sqrt{1 - \frac{1}{n^2}\frac{z^2}{z^2+d^2}}} \approx \frac{1}{(d^2 + z^2)^{\frac{3}{2}}}. \tag{2}$$

In this Section and in Section 4, this expression is used for the fitting of experimental and simulated data.
The experimental campaign has been conducted using a setup similar to the one employed in the energy-light calibration (see Figures 7 and 11a). The crystal light output has been measured from the central position to $z = 8.8$ cm, that is slightly more than maximum crystal-camera offset in OSCAR. Pictures have been taken with different exposure times, and then the light output has been properly averaged to reduce the experimental uncertainty. For this specific study, the sum of pixel values in the ROI has been used as the signal, instead of the MPV, in order to better compare the experimental data with simulations (discussed in Section 4), where the current of photons crossing the lens is scored. The response from crystals with different widths ($w = 0.2$, 0.3, 0.5, 1.0 cm) and materials (BGO and EJ-200) has been measured, to explore the influence of these parameters on the POV effect.
Experimental results are shown in Figure 11b. The empirical model well describes the experimental data, and the total RMS of residuals amounts to $\sigma_{\text{res}} = 2.87\%$, that is comparable to the experimental error. However, the distance obtained by the model fitting is different from the real one of $d = 12$ cm, that means that the physical

model proposed is too simplified. To save the empirical model, that will be useful in the following discussion, the real distance $d$ has been replaced by an "effective distance" $d_{\text{eff}} = d_{\text{eff}}(n, w, ...)$.
Currently, the response matrixes take into account of POV effect using correction coefficients obtained experimentally. However, it would be interesting to predict the POV curve shape and amplitude through Monte Carlo simulations, and this topic will be discussed in detail in Section 4.

## 3.2. SiPD Readout

Camera based data acquisition presents several problems:

- data post-processing difficult to automatize (ROI is user-defined);
- large noise variation over time (background must be measured before every shot, as described in Section 3.1.1);
- requires bulky light-tight setup;
- POV effects to be corrected (as described in Section 3.1.2).

A promising alternative to the CMOS camera is offered by the silicon photodiode (SiPD). This device converts the light signal coming from the crystal – to which it is attached through air coupling or optical grease – in an electronic signal. In addition to mitigating the above-mentioned problems, SiPD features an efficient light collection, fast time response and compact size [16], as shown in Figure 12.

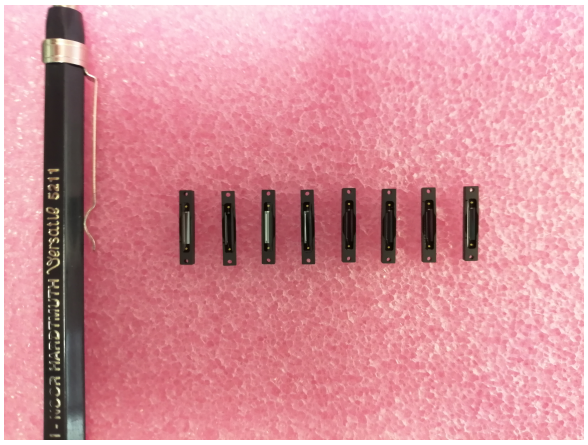

Figure 12: SiPD model S1337-BR adopted for the readout system.

For the OSCAR readout system, the suitability of the SiPD model S1337-BR provided by HAMAMATSU is being evaluated [30]. The photosensitivity curve of the chosen SiPD model well matches the emission spectrum of BGO and EJ-200 crystals, as shown in Figure 13, and so a good sensitivity to the scintillation light is expected.
The complete readout system for OSCAR will consist of an array of SiPDs, one for each crystal, all connected to the same multichannel pulse analyzer. However, at this preliminary stage, it is more useful to explore the capabilities of one single channel line, in order to find the optimal circuit design for the expected input signal, that is a short but very intense burst of light.

### 3.2.1 Electronic Hardware - Preliminary Evaluation

In a well-designed readout system, a crucial role is played by the electronic circuit that collects the signal from the SiPD and amplifies it. The design of amplifying circuits for these very specific applications is well described in literature [32, 33]. In this preliminary phase, it was decided to start from an existing SiPD amplifier circuit currently used for the diagnostic of laser beamlines at ELI Beamlines, and to adjust it for the detection of short and intense burst of photons coming from the scintillator. The front-end electronic circuit – that is the electronic hardware in between the SiPD and the analog-to-digital converter (ADC) – is the most influencing stage of the electronic scheme, since it processes the signal before the digitalization, and so noise levels and signal distortions should be carefully considered. In the proposed electronic scheme, the front-end circuit is composed by (see Figure 14):

- trans-impedence amplifier (TIA): amplifies and integrates the input signal;
- inverter amplifier: inverts the polarity and perform an amplification of the signal;
- peak holder: integrates and keeps the peak of the signal for a time long enough for the digitalization.

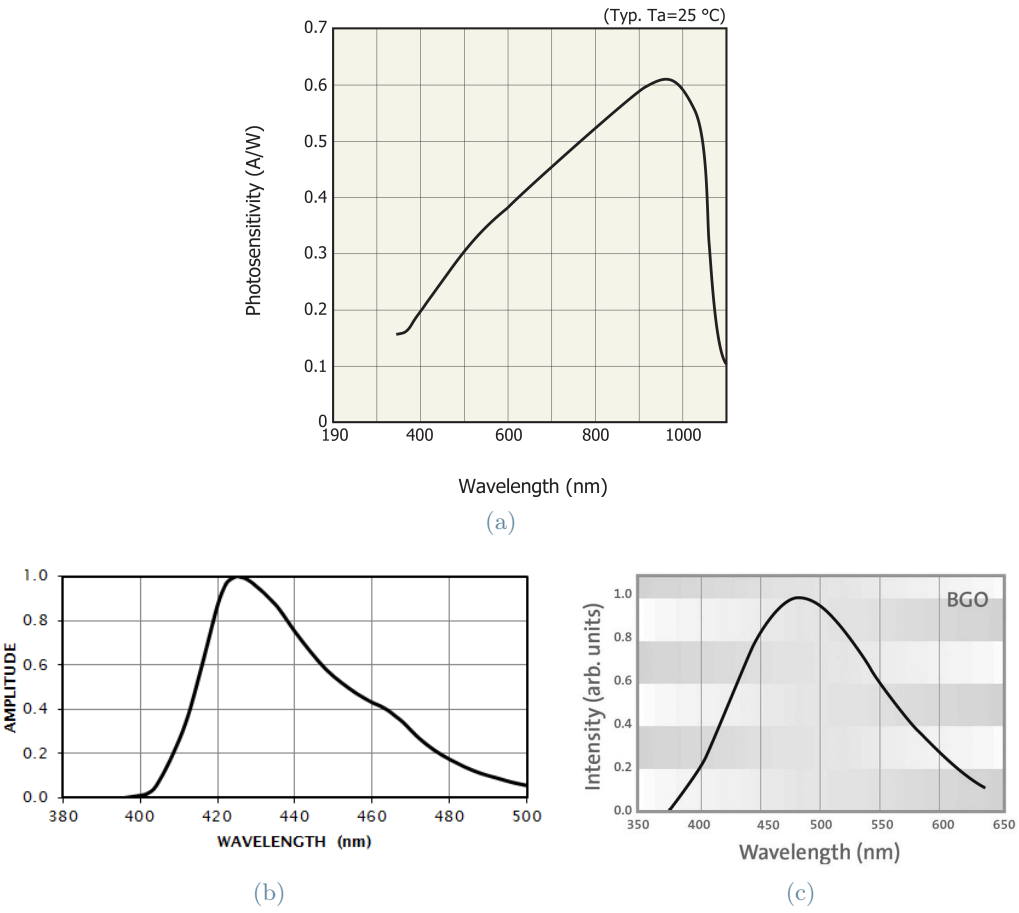


(a) (b) (c)

Figure 13: Photosensitivity spectrum for S1337-BR [30] (a), EJ-200 emission spectrum [21] (b), BGO emission spectrum [31] (c).

In order to analyze and adapt each of these macro-components to design requirements, LTspice XVII [34], a popular schematic-driven circuit simulation program, has been employed for evaluating the response in time to a pulse of current in input, and for estimating the noise level of the circuit. The SiPD has been modeled as a current source in parallel to a resistance and a capacitance, as suggested in literature [35]. The values for the resistance and capacitance are the ones suggested in the SiPD datasheet [30].

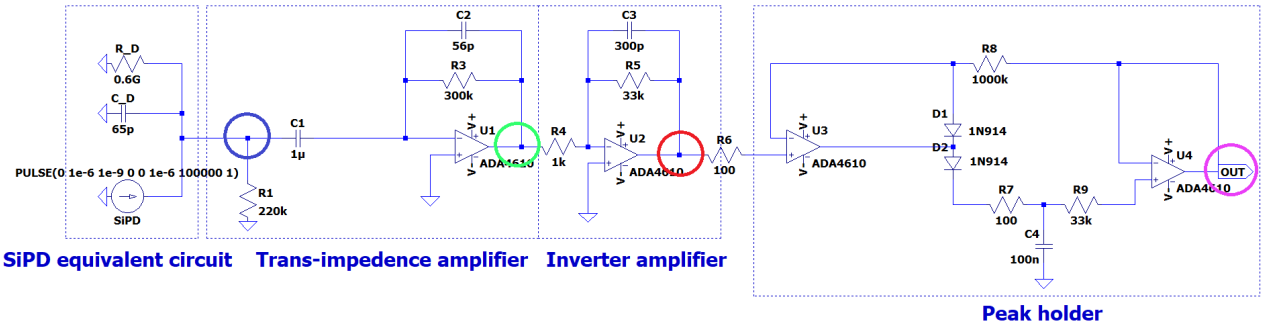


Figure 14: Front-end electronic circuit for the collection of the signal from the SiPD, tuned for the expected pulse of current of 1 µA for 1 µs.

As a first step in the analysis, the transient behavior of a 1 µs rectangular pulse of 1 µA current has been simulated. This signal corresponds to the expected charge of approximately 1 pC produced in the SiPD in one laser shot at ELIMAIA. The precise time structure of the input signal is not relevant in practice, since the signal is integrated in the first stages of the readout electronic circuit, as shown in Figure 15, where it is clear that

both the trans-impedence amplifier and the inverter amplifier act as low pass filter and integrator, and this is also evident from the AC analysis shown in Figure 16. Nevertheless, the pulse has been shaped with a duration of the same order of magnitude expected from a BGO crystal ($\tau = 300$ ns).

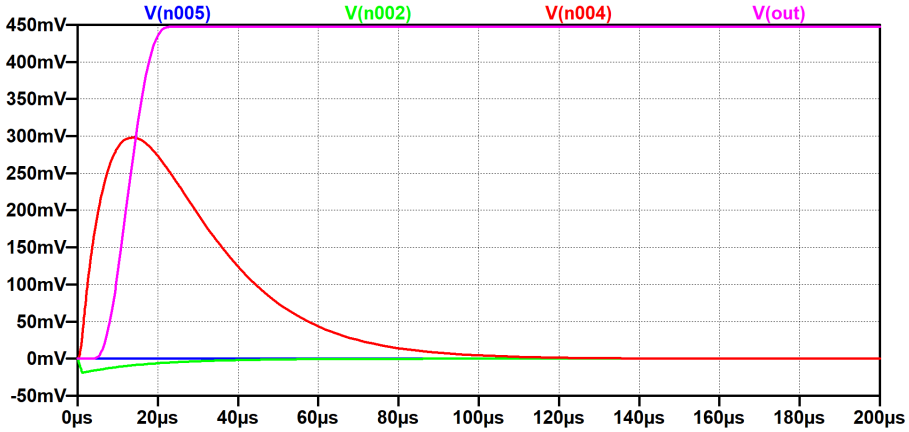


Figure 15: Voltage transient simulation of the readout electronic circuit with a pulse of current of 1 µA for 1 µs as input. Colors follow the respective node in Figure 14.

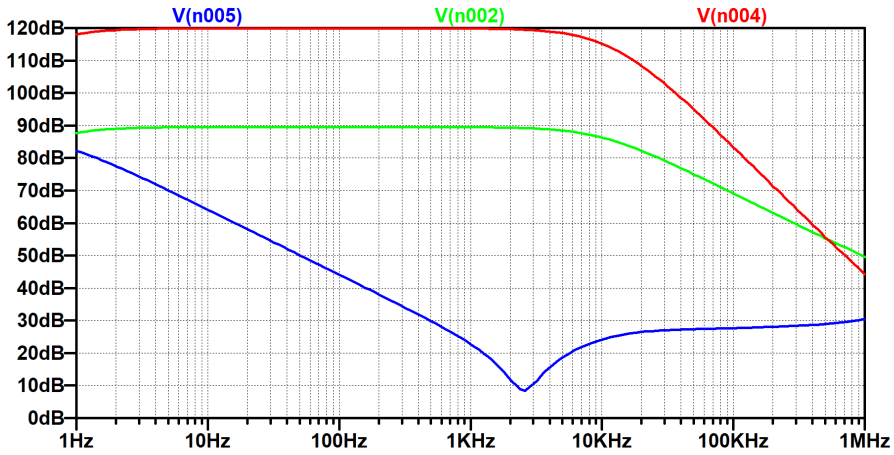


Figure 16: Bode plot for the readout electronic circuit. Colors follow the respective node in Figure 14.

The output signal reported in Figure 15 is obtained from the circuit shown in Figure 14, where few improvements have been performed with respect to the original electronic scheme in order to obtain, with the minimum number of new components:

- sufficiently high voltage at the output of the peak holder, in the order of mV-V, such that the signal can be read by the digitizer;
- wide linearity response in terms of output voltage in function of the deposited charge in the SiPD. The linearity range should be centered around the deposited expected charge of 1 pC;
- low electronic noise.

The improved circuit design was achieved proceeding by trial and error, and it provides an output signal of about 400 mV for 1 pC of charge in input. The linearity range extends for two order of magnitude around the expected input charge, as shown in Figure 17. This design will be a useful starting point for the next experimental sessions, where the electronic circuit and the SiPD will be tested using pulsed light from a laser diode: the comparison in between experimental data and simulations will eventually validate these simulations, and so it will be meaningful to perform a real circuit optimization through a more systematic procedure.
Minimization of the electronic noise is one of the design objectives. Different types of noise are present in an electronic circuit. Among them, thermal noise and flicker noise (also known as $1/f$ noise) are tipically the most dominant one [36]. LTspice XVII can perform frequency domain noise analysis, taking into account shot, thermal and flicker noise [34]. These two last components can be clearly recognized in Figure 18. The $1/f$ shoulder at low frequency is due to flicker noise, while the portion of the spectrum at higher frequencies is related to thermal noise [36]. For the simulation, a maximum frequency of 10 kHz has been chosen, since 10kHz is the cut-off frequency of the filter placed in between the peak holder and the digitizer.

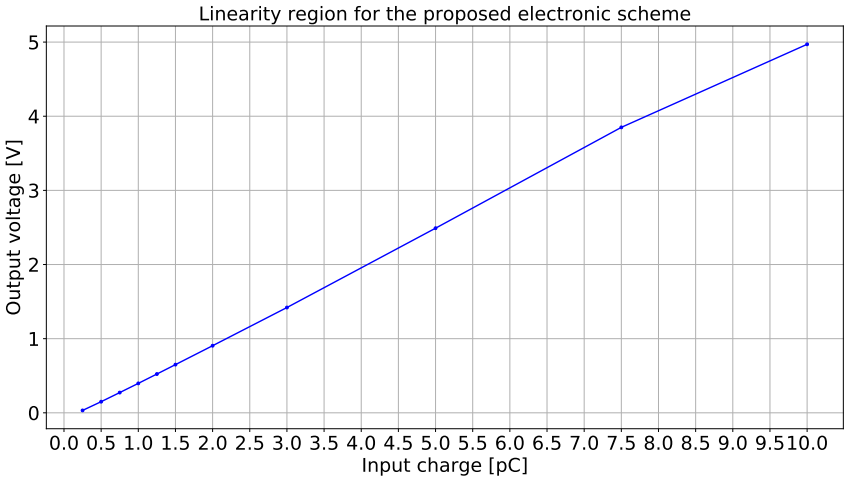


Figure 17: Input charge - output voltage curve for the electronic scheme obtained from simulations.

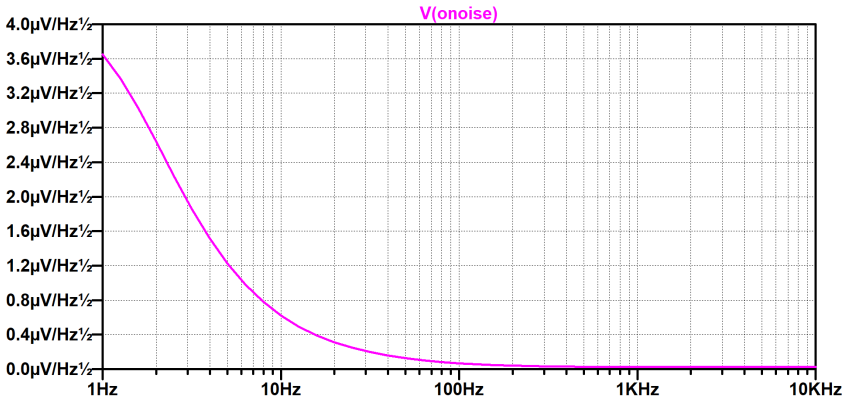


Figure 18: Simulated noise density at the output of the readout electronic circuit.

As a final remark, it is important to be aware of the electromagnetic pulse (EMP) generation from the laser, which could lead to damages to electronic components inside and outside the interaction chamber. There are three main mechanisms producing EMP [37]:

1. chamber resonating at its natural frequencies in MHz domain;
2. antenna radiation excited by the transient return current in the holder of the target, in the GHz domain (electrons ejected from the target induce a return current from the chamber to the holder of the target);
3. emission of THz radiation by the jets of hot electrons produced in target.

Electronics installed around the interaction chamber must be protected against EMP, and so the electronics of OSCAR, both when using CMOS camera or the SiPD.
In the current readout system for OSCAR, the CMOS camera is protected from EMP by the metallic case of the camera itself, that is EMP resistant and acts as a Faraday cage. In case SiPDs are used as readout system, everything is enclosed in a metallic box, and radiation reaches the array of scintillators through an aluminized Mylar window, that ensures the continuity of the conductivity in the Faraday cage.

## 4. Simulation of Optical Photons Propagation

Optical simulations allow predicting the propagation of optical photons in space and time. A refined optical model for OSCAR would be helpful in predicting the response of the crystals in terms of visible light output, that is the experimental quantity observed in practice. In general, the propagation of optical photons in matter is far from being an easy topic in physics, and Monte Carlo techniques offer a valid approach to this problem.
As any other physical simulation, optical simulations are based on certain physical models that describe the propagation of optical photons in matter accounting for the optical properties of:

- surfaces: reflection mechanisms, reflectivity, etc.
- materials: index of refraction, geometry, attenuation coefficient, etc.

Reflection mechanisms especially deserve a further comment, since optical models that are presented in the following sections have been developed with the aim to improve this aspect in particular. When a photon encounters a different media along its travel, it could be either absorbed, transmitted or reflected with a certain probability that is described by the coefficients of absorption, transmission and reflection (also known as reflectivity). In case the photon is reflected, four main mechanisms drive the reflection of light from a generic non-smooth surface [38]:

1. specular spike: the photon undergoes mirror reflection, that means that the angle of reflection is equal to the incident angle;
2. specular lobe: the photon is reflected at a random angle following a Gaussian distribution centered at the specular direction of reflection;
3. backscatter: the photon is reflected at a random angle following a Gaussian distribution centered at the direction of origin of the photon;
4. diffuse lobe (Lambertian reflection): the photon will be reflected with a Lambertian distribution probability, i.e. following a cosine distribution around the normal of the surface [39].

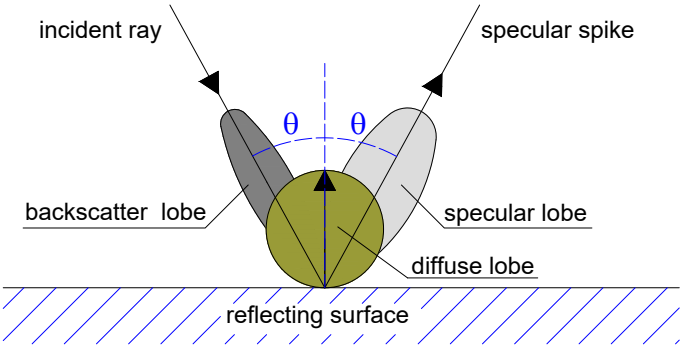


Figure 19: Four main mechanisms of reflection of light from a reflecting surface.

The reflector wrapped around the scintillation material is characterized by a very high reflectivity, and a small fraction of photons is absorbed in the material, while no photons are transmitted. Instead, when the photon goes from crystal to air there is not any absorption, but only transmission and reflection. In this case, Fresnel equations can be used to estimate the reflectivity ($R$) in function of the angle of polarization (parallel or perpendicular to incident plane), the incident angle ($\theta_i$), and the indexes of refraction ($n_i$ and $n_t$) of the two transparent media [40]:

$$R_{\parallel} = \left( \frac{n_i \sqrt{1-\left(\frac{n_i}{n_t}\sin\theta_i\right)^2} - n_t \cos\theta_i}{n_i \sqrt{1-\left(\frac{n_i}{n_t}\sin\theta_i\right)^2} + n_t \cos\theta_i} \right)^2, \; R_{\perp} = \left( \frac{n_i \cos\theta_i - n_t \sqrt{1-\left(\frac{n_i}{n_t}\sin\theta_i\right)^2}}{n_i \cos\theta_i + n_t \sqrt{1-\left(\frac{n_i}{n_t}\sin\theta_i\right)^2}} \right)^2.$$

In the optical models that are presented in the following sections, the light is assumed to be non polarized, and so the Fresnel reflectivity is estimated as the average value of reflectivity between parallel and perpendicular polarization:

$$R = \frac{1}{2}(R_{\parallel} + R_{\perp}).$$

From Fresnel equations, it should be noticed that for an incident angle $\theta_c = \arcsin(\frac{n_t}{n_i})$ with $n_i > n_t$ the reflectivity goes to one, that is total reflection. This angle is called critical angle.
Optical simulations in FLUKA.CERN code have been performed using various optical models, described in Sections 4.2, 4.3, 4.4. Results of simulations are reported in Sections 4.5 and 4.6, where the POV effects and the time straggling of photons inside the crystal have been investigated.

## 4.1. Optical Simulations in FLUKA.CERN code

The physics of propagation of photons in matter in FLUKA.CERN code is implemented at a very elementary level: all the interfaces in between different materials are assumed to be smooth surfaces, and so only specular reflection can occur. A user routine called FRGHNS could be used to introduce a specular Gaussian lobe at reflection, but this is typically not accurate enough to properly describe the reflection on a non-smooth surface. In the specific case of OSCAR, the $TiO_2$ paint and the PTFE tape reflector are diffuse (Lambertian) reflectors [41, 42], and it would be impossible to reproduce this specific reflection mechanism in the simulations using the

FRGHNS routine. For all these reasons, two new optical models have been developed and implemented using user routines into the FLUKA.CERN code.
Overall, three models have been explored for optical simulations with OSCAR:

- "Ideal" model: specular reflections and crystal-air reflectivity calculated through Fresnel equations.
- "LUT" model: reflection on the reflector layer is simulated through experimental look up tables (LUT). The crystal-air reflectivity is calculated through Fresnel equations, and a refraction lobe is simulated at the interface in between crystal and air.
- "Detailed" model: all the four reflection mechanisms – specular spike, specular lobe, backscatter and diffuse reflection – described in the previous Section are simulated. The crystal-air reflectivity is calculated through Fresnel equations, and a refraction lobe is simulated at the interface in between crystal and air.

The ideal model is the only one among the three to be already implemented in the FLUKA.CERN code, since it is the default FLUKA.CERN treatment. To include the LUT and detailed models in the code, custom USRMED user routines have been developed. USRMED is called from the input file and allows dealing with direction changes and absorption processes.
The experimental POV curves reported in Section 3.1.2 have been used as a benchmark for the three models: the goal was predicting the POV curve shape (see Figure 11b), with a uniform "scale factor" among different crystals. The scale factor $S$ is defined as the ratio between the measured and simulated POV curve amplitude, and it is calculated through a least-square minimization where $S$ is the free parameter. In other words, the scale factor is defined as the number $S$ that minimizes the sum:

$$\sum_{i}^{N} \frac{(\sum \text{p.v.}|_{\text{i-th position}} - S \cdot I_{\text{sim.}}|_{\text{i-th position}})^2}{\epsilon_i^2}$$

where:

- $N$ is the total number of pictures taken with the same crystal, in different positions $i$ with respect to the camera;
- $\sum$ p.v. is the sum of pixel values in the ROI (subtracted by the background) for the picture with the crystal in i-th position;
- $I_{sim}$ is the current of optical photons scored in simulations, in an equivalent lens surface placed at the i-th position;
- $\epsilon_i$ is the error related to the $\sum$ p.v., since the error related to the $I_{sim}$ is negligible in comparison.

The scaling factor should be independent on the crystal properties, while it should be dependent only on the various and unknown parameters of the camera.
The same model used for energy-light calibration, shown in Figure 7 and described in Section 2, has been employed to perform POV simulations. Optical photons produced in the crystal are propagated in the surrounding air, and the output of the simulation is the current of photons crossing 24 circular surfaces with a diameter equal to the one of the camera lens (about 2.7 cm). These surfaces are placed at a distance $d = 12$ cm from the face of the crystal, and their axis are at various distances $z$ from the axis of the crystal, in order to estimate the light collected from the camera placed in various positions with respect to the crystal axis. Different optical models lead to different spatial distribution of photons inside and outside the crystal, and so to different values of current crossing the circular surfaces. The FLUKA.CERN scorer USRBDX has been used to estimate the current of optical photon through the circular surfaces.
Before going on more in the details of the models and on the results of simulations, it should be recalled that optical properties of materials, as reflectivity and refraction index, also depends on the wavelength of the photon, and since the emission spectrum of BGO and EJ-200 crystals spans over tens of nm, this should be taken into account in the optical model. However, the wavelength dependencies are expected to have a higher order impact on results with respect to reflection mechanisms, and so they have been neglected, together to absorption and diffusion phenomena, since the length of the trajectories of photons inside the crystals is orders of magnitude lower than the characteristic length of these phenomena ($\approx$ m), as it will be shown in the Section 4.6. Hence, for the BGO and EJ-200 the values of $n_{BGO} = 2.15$ and $n_{EJ-200} = 1.58$ have been used in the simulations [16], although these values could be subjected to small deviations from one crystal to the other, other than depending on the wavelength of the light.
As a final remark, a qualitatively first sight comparison among the three models is reported in Figure 20. In this illustrative simulation, the source of optical photons is centered on the red circle and photons are emitted as a pencil beam towards the front face of the crystal (the one on the right in the view). Once photons reach the crystal-air interface, they are partially reflected and partially refracted. The portion of the beam reflected goes back toward the center of the crystal, and then it is again reflected or absorbed in the reflector.
In the ideal model, photons are not diffused in reflection/refraction, while with the newly proposed models the photon beam is spread every time it reaches an optical surface, and in the end photons are everywhere inside and outside the crystal.

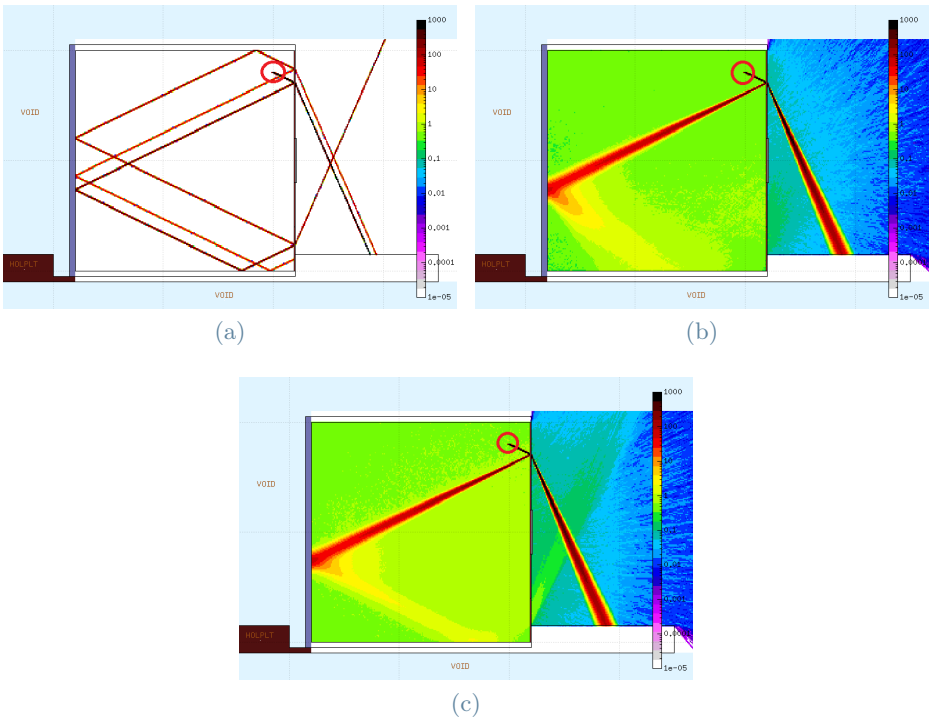


(a) (b)

(c)

Figure 20: Optical photon fluence inside the crystal obtained with ideal model (a), LUT model (b), detailed model (c). In this simulation, an optical photon beam is emitted from the center of the red circle, with a certain direction towards the front face of the crystal.

## 4.2. Ideal Model

In the ideal model, specular reflection is the only reflection mechanism possible, and reflectivity at the crystal-air interface is assessed through Fresnel equations, while the reflectivity of PTFE is user defined. In practice, in POV simulations the reflectivity played a role similar to a fitting parameter, and it has been adjusted to achieve the best fit in between experimental and simulated POV curve. Since there is only this parameter to tune in the simulation, a procedure to achieve the best fit can be easily defined:

1. The simulated POV curve is obtained for different values of the reflectivity $R$, for different crystal widths and materials.
2. The empirical model described in Section 3.1.2 is fitted to each of these simulated curves to obtain a best-fit parameter $d_{eff}$.
3. The curve of $R$ as a function of $d_{eff}$, called the characteristic curve, is obtained by fitting the points found from simulations to a degree-2 polynomial, as shown in Fig. 21a where the characteristic curve for the BGO crystal 1.0 cm width is reported.
4. The best-fit parameters $d_{eff}$ obtained from the experimental POV curves are input to the respective characteristic curve, to obtain a crystal-specific reflectivity $R'$.
5. A new simulation is run using the reflectivity $R'$ derived from the characteristic function. The simulation results are then compared to the experimental data as shown in Figure 21b, where the comparison in between simulated POV curve and experimental data for a BGO crystal 1.0 cm width is reported.

One of the advantages of this method is that it is immediate to assess the reflectivity of the PTFE wrapping from a POV curve measurement, once the characteristic function is available.
The impact of $R$ on the POV shape and amplitude is shown in Figure 22. As expected, the absolute intensity seen by the camera increases with the reflectivity. In addition, having a higher number of photons that are reflected spreads the distribution of photons incident on the crystal-air surface facing the camera; this results in a wider distribution of the outcoming photons. This effect is apparent on the normalized POV curves.
Concerning the index of refraction, the amplitude of the curve is expected to change in function of $n$, since an increase in $n$ leads to a decrease in the value of the critical angle, hence a higher probability for the photon to be totally reflected at the crystal-air interface facing the camera, and so being absorbed in the reflector. This is in agreement with the curves shown in Figure 23: a variation in $n$ leads to a change on the amplitude and not on the shape of the curves.
As a final remark, it is interesting to notice in Figure 24 how the refraction angle distribution is the one typical

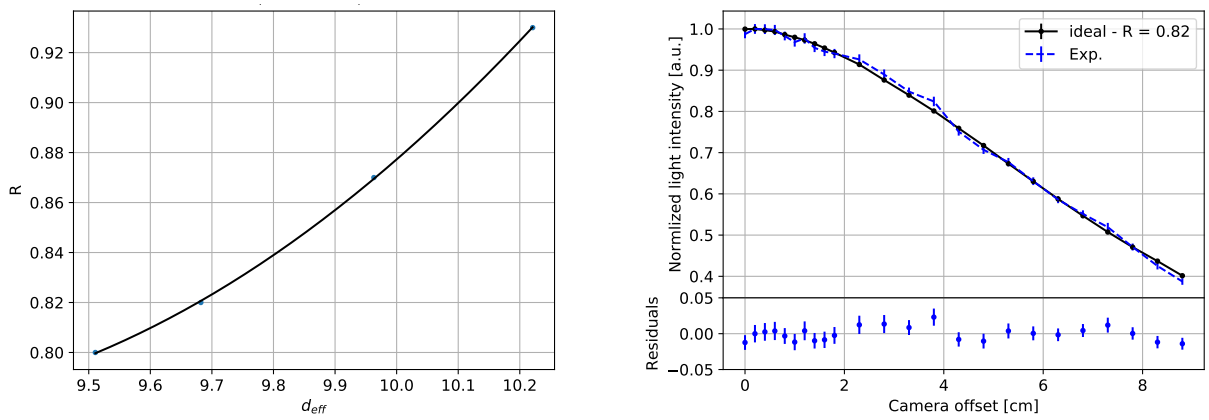


(a) (b)

Figure 21: The characteristic function (a) and simulation results compared to experimental data (b) for BGO crystal 1.0 cm width. Simulation performed using the ideal model.

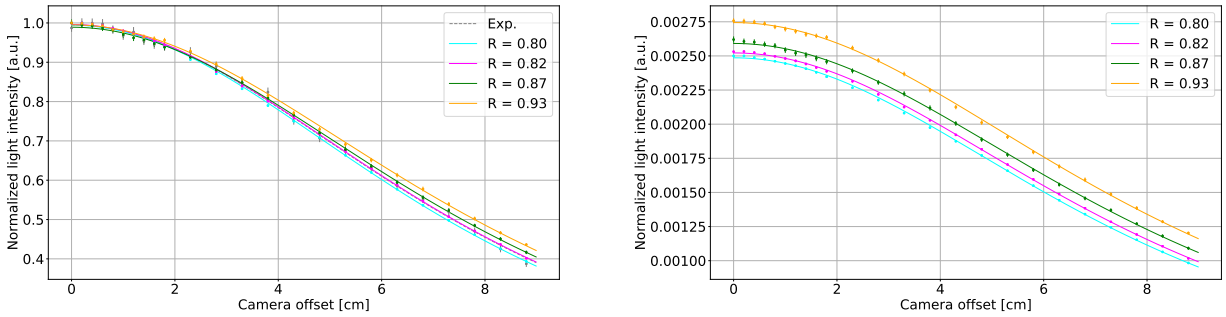


(a) (b)

Figure 22: The normalized (a) and absolute (b) simulated POV curves for different values of $R$ using ideal model on a BGO crystal, 1.0 cm width, $n = 2.15$.

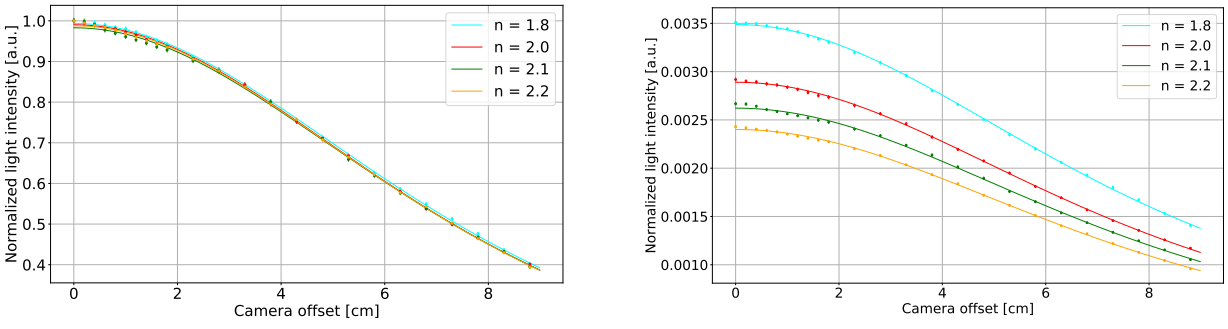


(a) (b)

Figure 23: The normalized (a) and absolute (b) simulated POV curves for different values of $n$ using the ideal model on a BGO crystal, 1.0 cm width, $R = 0.82$.

of a quasi-Lambertian emitter, and this is in agreement with the work performed by G. Haak et al. [43]. For a "generalized" Lambertian emitter/reflector, the angular distribution of rays is expressed as:

$$\frac{dP(\theta)}{d\theta} = \int_0^{2\pi} cos^{\alpha}(\theta) sin(\theta) d\phi \propto cos^{\alpha}(\theta) sin(\theta)$$

where $P$ is the light power, $\theta$ the polar angle of emission, $\phi$ the azimuthal angle of emission, and $\alpha$ is a correction to the cosine term; when $\alpha = 1$, the distribution is a pure Lambertian one.

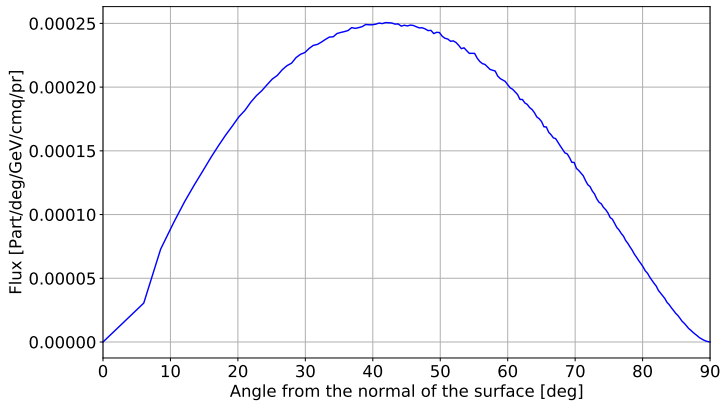


Figure 24: Refraction angle distribution for a BGO crystal, 1.0 cm width, R = 0.80.

## 4.3. LUT Model

The LUT model makes use of experimental data collected in the so-called "Look Up Tables" (LUT) [38, 44]. These experimental tables describe the distribution of photons reflected from a surface of a crystal with various finishes, i.e. etched surface, polished, etc... coupled with a reflector layer. An algorithm was developed using these data to more realistically model the photons reflected at the PTFE layer with respect to the ideal model. The look-up-tables are part of the Geant4 library, but they are not available in FLUKA.CERN, and so a specific user routine has been developed in order to read the experimental tables, and accordingly propagate photons in FLUKA.CERN.

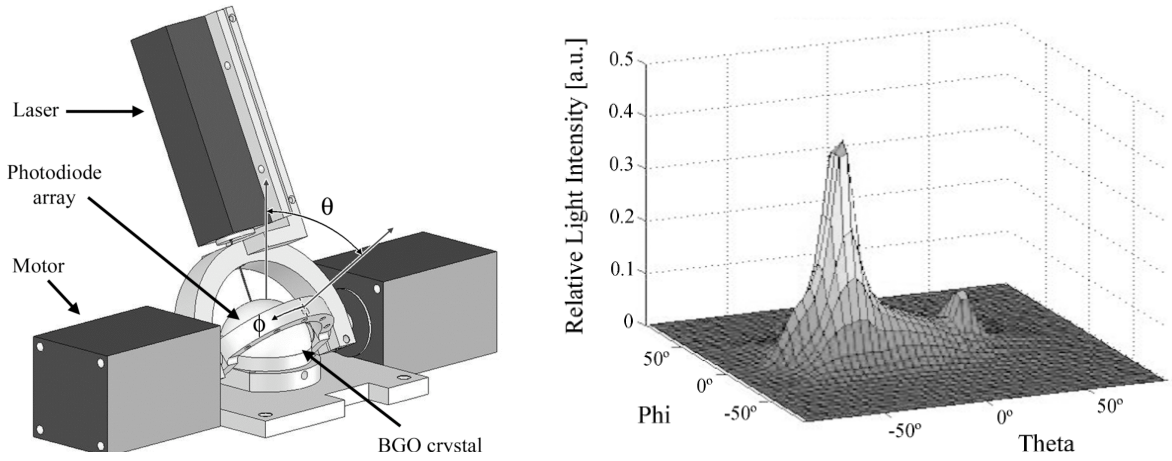


(a) (b)

Figure 25: Experimental setup used for measuring the reflection distribution from the crystal surface (a), and graphical representation of one of the distribution measured (b) [44].

LUT data were obtained experimentally using the setup shown in Figure 25a: a laser beam impinges on a hemisphere of BGO crystal with a layer of reflecting material on the bottom plane surface, and a detector measures the intensity of light at different angles $\theta$ and $\phi$ in function of the incident angle of the laser beam [44]. A representative outcome of this experimental measure is plotted in Figure 25b, where it is possible to recognize the specular lobe (the main peak) and the backscatter lobe.
Since the reflected light was measured at discrete values of incident angles and reflected angles $\theta$ and $\phi$, with steps of 1°, 4°, 5° respectively [44], the LUT tables covers only a discrete set of combinations of angles. To overcome this limit, that could lead to discretization effects, the LUT have been extended to a continuous range of values through a bilinear interpolation. The result of this operation is shown in Figure 26.
The lookup algorithm proceed as follows: when the photon encounters the reflector layer, and it is not absorbed, it is reflected with a direction that follows the distribution described by the LUT. On the contrary, when the photon reaches the crystal-air interface, it is refracted or reflected at a random angle following a Gaussian distribution centered at the directions defined by the Snell's law in the case of refraction and specular reflection in the other case (see Figure 28b). This refraction/reflection lobe mimics the effect of a non-smooth surface,

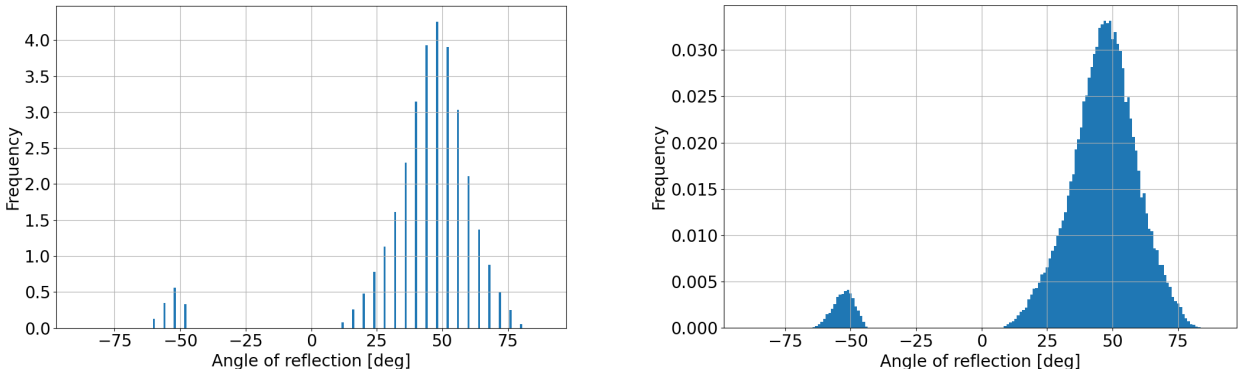


(a) (b)

Figure 26: Comparison in between $\theta$ distributions for an incident angle of 50° from LUT (a) and interpolated LUT (b).

and the width of the Gaussian distribution is defined using reasonable values, since an experimental dataset is not available. The reflectivity at the crystal-air interface is calculated through the Fresnel equations.
For the simulations of the POV effect, the LUT dataset for etched surface and PTFE as reflector has been used, as it corresponds the best to the scintillators used for the POV measurements. The width of the Gaussian refraction/reflection distribution at the crystal-air interface has been set equal to zero, since the front face of the crystal is polished, and so a wide broadening of the photon distribution due to refraction is not much expected. Therefore, the only parameter to be tuned in the simulation is the reflectivity $R$, as for the ideal model; the same process based on the characteristic function $R$ - $d_{eff}$ has been used for assessing the value of $R$ that leads to the best fit among experimental and simulated POV curves. In Figure 27b the comparison in between experimental data and results from simulation for a BGO crystal 1.0 cm width is reported.

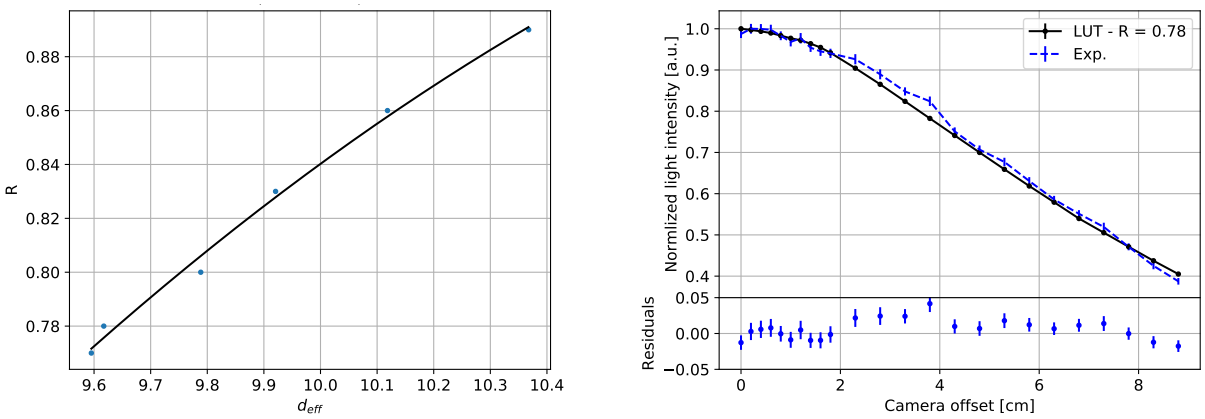


(a) (b)

Figure 27: The characteristic function (a) and simulation results compared to experimental data (b) for BGO crystal 1.0 cm width. Simulation performed using the LUT model.

## 4.4. Detailed Model

In the detailed model, photons are reflected according to the four mechanisms described at the beginning of the section: sthe specular peak reflection, specular lobe reflection, backscatter reflection and Lambertian (diffuse) reflection. In particular, the model has been tailored for a crystal wrapped in a PTFE tape; in fact, it has been supposed that in between the crystal and the reflector tape there is a thin layer of air (see Figure 28a), and from this assumption the algorithm has been developed following the scheme reported in Figure 29. It should be noticed that in the case the photon reaches the reflector and it is not absorbed, it will be reflected following a Lambertian distribution, otherwise it will be reflected from the crystal-gap interface following the four reflection mechanism, each one with a certain probability. A refraction lobe (see Figure 28b) has been also included in the algorithm for the surface without the reflector (see Figure 30), mimicking the effect of roughness. However,

the width of the Gaussian lobe is expected to be very low for the reasons already explained in Section 4.3. The reflectivity at the crystal-air interface is calculated using the Fresnel equations.

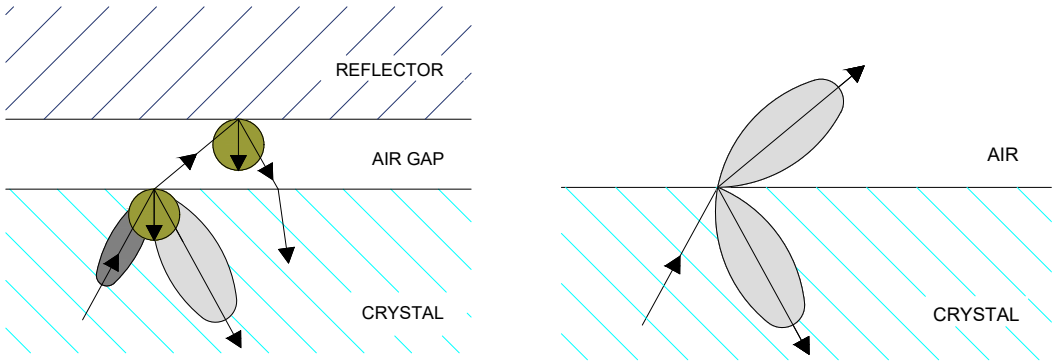


Figure 28: Reflection dynamics in detailed model (a), and refraction dynamics in LUT and detailed models (b).

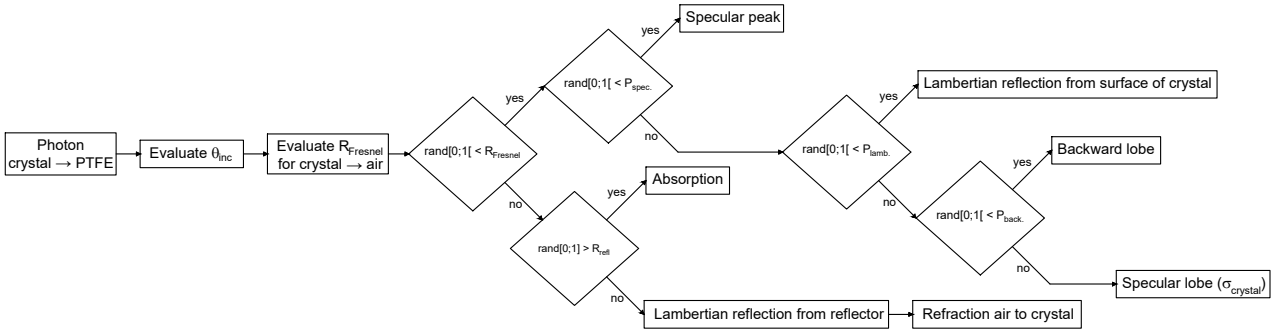


Figure 29: Algorithm for the reflection at the crystal-reflector interface in the detailed model.

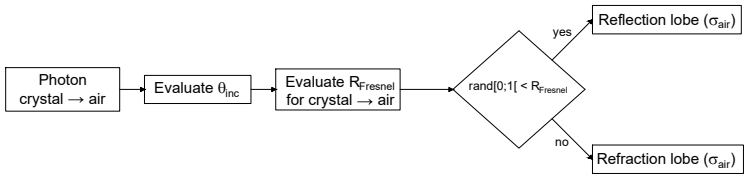


Figure 30: Algorithm for the reflection at the crystal-air interface in detailed and LUT models.

The detailed model has seven free parameters to be defined:

- $R$: reflectivity of the reflector.
- $n$: index of refraction.
- $P_{\text{spec.}}$: probability of specular reflection at the crystal-gap interface.
- $P_{\text{lamb.}}$: probability of Lambertian reflection at the crystal-gap interface.
- $P_{\text{backw.}}$: probability of backward reflection at the crystal-gap interface.
- $\sigma_{\text{crystal}}$: width of the specular lobe in crystal-reflector reflection.
- $\sigma_{\text{air}}$: width of the lobe in crystal-air refraction/reflection.

The higher number of free parameters to tune with respect to the previous models results in a more flexibility in fitting the POV experimental data, but it is also much more difficult to find the set of parameters that leads to the best fit. To help the optimization, some constraints have been defined on the basis of physical

considerations: for example, it would be expected that the scaling factor is the same for all the crystals (see Section 4), and that all the parameters except $R$ and $n$ are independent on the crystal width and material, since they should eventually depend only on the surface characteristics. However, it is not guaranteed that the etched faces covered with PTFE tape have the same quality of the finishing, and so small deviations of these parameters from one crystal to another could be accepted.
The simplest approach is to perform a trial-and-error optimization, the results of which are shown in Table 2. The blue color underlines that the same or similar values of the parameter were found among different crystal setup. On the other hand, the red color remarks unexpected values for the parameters. More precisely, the $P_{spec}$ was expected to be the same for all the crystal setup, as explained in the previous paragraph, and the $R$ found for BGO w = 0.5 cm is surprisingly small.

| Best fit parameters in detailed model | | | | | | | |
|---|---|---|---|---|---|---|---|
| | $n$ | $R$ | $P_{spec}$ | $P_{lamb}$ | $P_{backw}$ | $\sigma_{crystal}$ | $\sigma_{air}$ |
| BGO w = 0.2 cm | 2.15 | 0.95 | 0.54 | 0.9 | 0.2 | 0.10 | 0.001 |
| BGO w = 0.3 cm | 2.15 | 0.99 | 0.60 | 0.9 | 0.2 | 0.10 | 0.001 |
| BGO w = 0.5 cm | 2.15 | 0.65 | 0.50 | 0.9 | 0.2 | 0.10 | 0.001 |
| BGO w = 1.0 cm | 2.15 | 0.95 | 0.30 | 0.9 | 0.2 | 0.10 | 0.001 |
| EJ-200 w = 1.0 cm | 1.58 | 0.90 | 0.45 | 0.9 | 0.2 | 0.10 | 0.001 |

Table 2: Best fit parameters found through trial-and-error optimization process for various crystal setup. Simulations performed using the detailed model.

It should be stressed that the trial-and-error process doesn't guarantee reaching the best set of parameters, and so the values of the reflectivity assessed could be even very far from the real ones. Nevertheless, $R = 0.65$ found for BGO w = 0.5 cm is not even completely absurd, since there could have been some damages in the reflector tape that lead to an important leak of photons, and so a result like that should not be discarded a priori, but not even taken without the necessary attention, since there could exist another set of parameters with a better POV simulated curve and a more reasonable reflectivity value, that has not been found in the trial-and-error research. For this reason, a more systematic procedure for finding the parameters is needed.
In Figure 31 the comparison in between experimental data and results from simulation for a BGO crystal 1.0 cm width is shown.

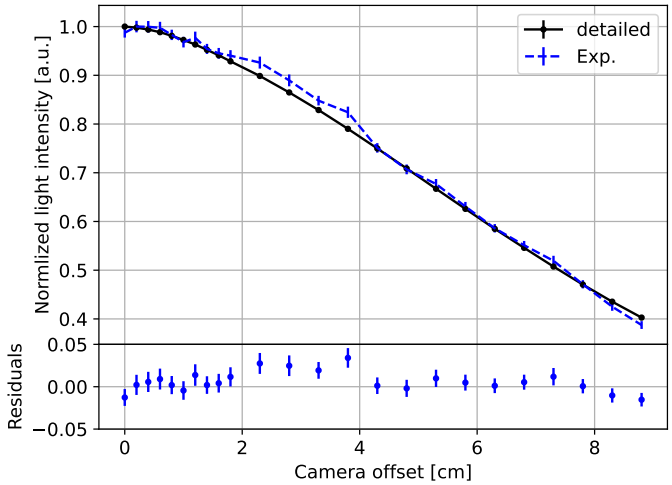


Figure 31: Simulation results compared to experimental data for BGO crystal 1.0 cm width. Simulation performed using the detailed model.

## 4.5. Optical Model Comparison

For each of the measured POV curve, a FLUKA.CERN simulation using each of the three models described earlier has been performed. Measurements and simulation results have been compared using the following metrics:

1. root-mean-square value (RMS) of the differences in between the experimental and simulated normalized POV curves, shown in Figure 32;
2. scale factor defined in Section 4, shown in Figure 33;
3. single-core computational time per simulated primary[1], shown in Figure 34.

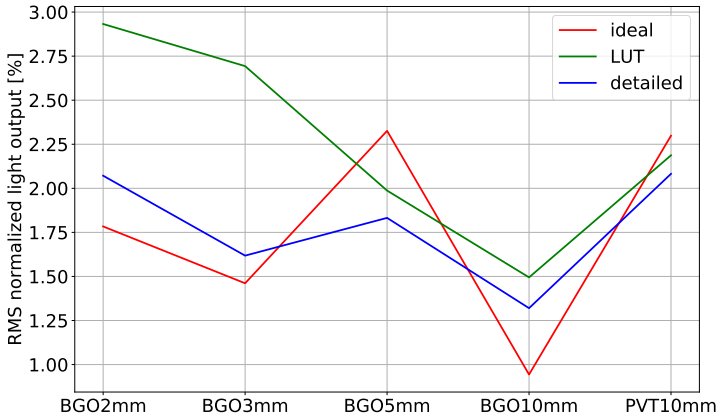


Figure 32: Root-mean-square value (RMS) of the differences in between the experimental and simulated normalized POV curves, for different optical models and crystal setup.

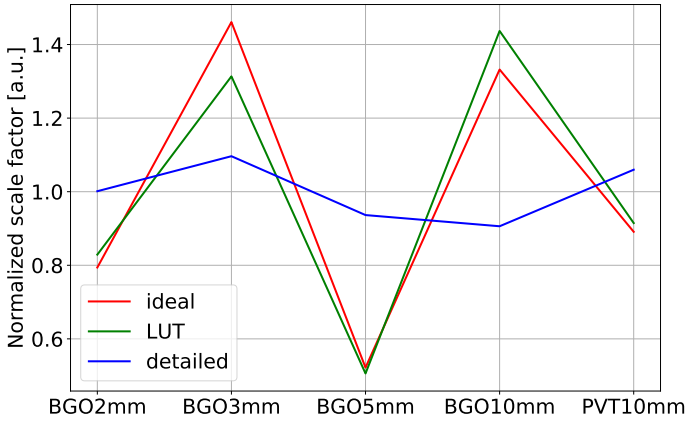


Figure 33: Normalized scale factor, for different optical models and crystal setup.

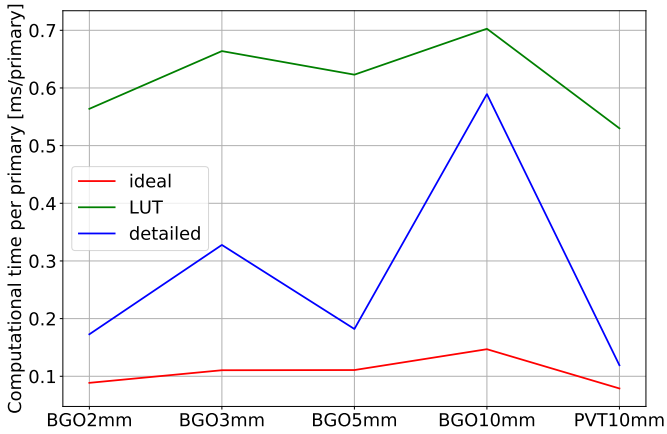


Figure 34: Computational time per primary simulated, for different optical models and crystal setup.

The three models presented a comparable performance concerning the RMS of the residuals, except for the LUT model which gave the worst RMS values for smaller crystals. However, it should be noted that even in

[1]Computational time comparison performed on a six-core Intel Core i7-8750H CPU @3.20 GHz with 16 GB RAM, but only one core has been used in the simulations.

the worst case, the RMS value is approximately 3%, that is still compatible with the experimental error on the POV curve points.
For the scaling factor, the detailed model achieved more uniform values, thanks to the higher number of fitting parameters.
The simplest model is, as expected, also the fastest one; the computational time for the LUT is the highest one, mainly due to the slow angle lookup algorithm. However, there is still room for improvements on this aspect of the new models, that have not been optimized for speed performance yet.
Finally, it is interesting to compare the values of PTFE reflectivity assessed through the fitting procedure. As shown in Figure 35, ideal and LUT models are quite in agreement on the reflectivity values, while the detailed model is far from them, and this could be a symptom of a convergence to a non-optimal solution, as previously explained.

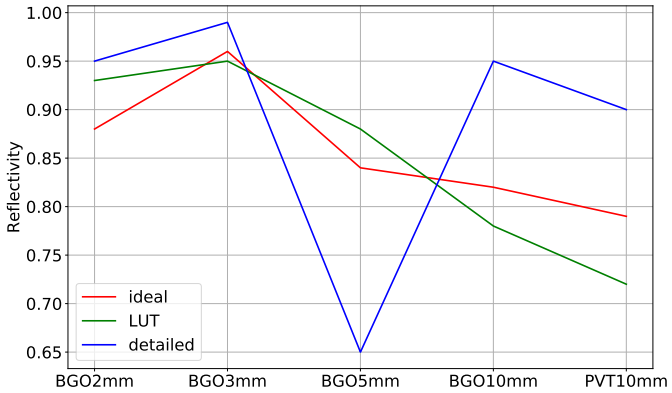


Figure 35: PTFE reflectivity values obtained through the fitting of the simulation results to experimental data.

## 4.6. Time Evolution of the Light Signal

Having developed sophisticated optical models, it would be interesting to perform optical simulation studies different from the POV curve prediction. For example, it would be important to evaluate the time straggling of photons due to their propagation inside the crystal after their generation. In fact, it is known from Section 2 that there is a characteristic time for the scintillation event, but in addition to this time component, photons will travel inside the crystal before exiting the crystal. The overall time distribution of the light signal collected by the readout system will be therefore the convolution of the scintillation time and the straggling distribution, and this will be important for time-resolved measurements (as it will be proposed for the detection of neutrons, see Section 5).
In order to isolate the effects on the photon propagation on the time straggling, scintillation light in simulations has been assumed to be instantaneous ($\tau = 0$), and through the user routine MGRDRAW the time distribution of optical photons has been assessed for different values of reflectivity, crystal widths and indexes of refraction. Simulations have been performed using the LUT model, and results are shown in Figure 36.
It can be noticed that the most influencing parameter is the reflectivity: an increase in the reflectivity goes with an increase in the number of photon escaping from the crystal, and more precisely the additional photons that escape are the ones that have been subjected to more reflections, and so that spent more time inside the crystal. This effect translates to a distribution with a larger contribution from the tail.
In addition, the wider the crystal, the longer the travel for photons, hence the longer the time spent by the optical photons inside the crystal.
Finally, it can be also noticed that the lower the index of refraction, the shorter in time the distribution, since the speed of light in the crystal is higher.
The time distributions found are not surprisingly shaped as the superimposition of a Gaussian and an exponential distribution, as often observed in this kind of phenomena [16]; what is more counter-intuitive is the small bump after the main peak at around 0.5 ns. To better understand the origin of this bump, it is useful to analyze the time distribution in function of the number of reflections on the reflector reported in Figure 37. Photons with no reflections directly escape from the crystal, and no bump is observed, while photons with one or more reflections are characterized by a time distribution with the bump. This could be explained observing that for the same number of reflections on the reflector – and so, the same probability of escaping from the crystal – there could be two "modes of propagation" inside the crystal: the photon could be reflected on the reflector,

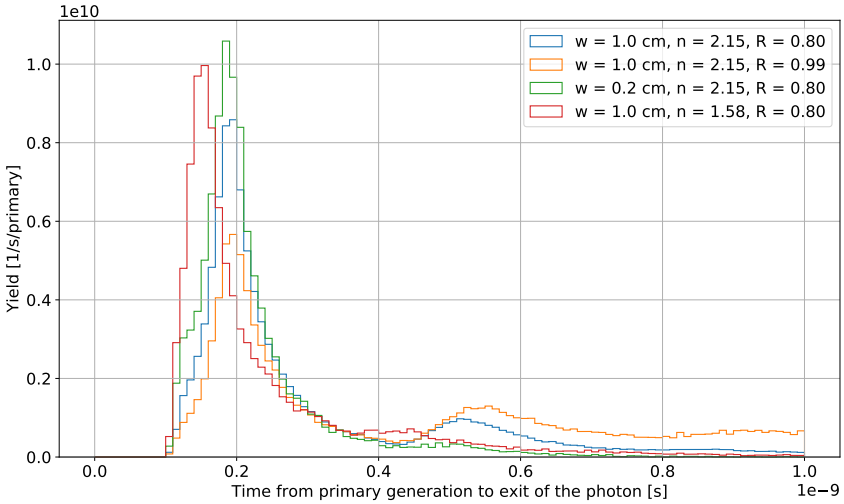


Figure 36: Time distribution (from the primary generation to the crossing of the crystal-air boundary by the optical photons) of the light signal from a BGO crystal, 1.0 cm width, using LUT model.

and then it goes out, or it could be at first reflected on the front face by internal reflection, then reflected on the reflector, and finally it goes out. This second mode will be characterized by a longer time, and so the bump. Two modes of propagation are also found analyzing the trajectories in space of photons with a fixed number of reflections on the reflector, as shown in Figure 38.

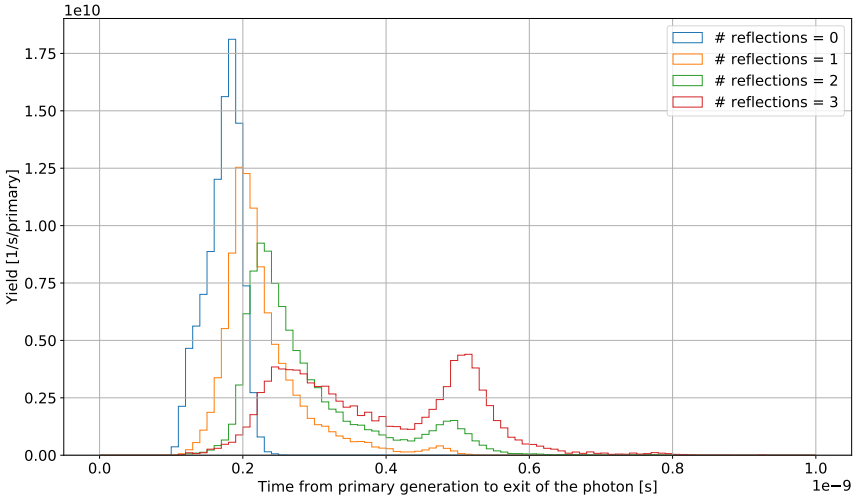


Figure 37: Time distribution of the light signal from a BGO crystal, 1.0 cm width, using LUT model. Each curve is related to a different number of reflections on reflector to which the photon has been subjected.

The time straggling is of the order of 1ns, that is negligible with respect to the characteristic scintillation time of BGO, but it is comparable to the characteristic time of EJ-200. Therefore, it could be an important effect to take into account in the development of a measuring system based on pulse-shape discrimination, for example. As a final comment, it is interesting to see how half of the signal – more precisely, 56% of the counts reported in Figure 37 – comes from photons that have been subjected to less than two reflection inside the crystal. For this reason, effects like absorption or diffusion in the crystal, with characteristic lengths of the order of meters [16], can be neglected.

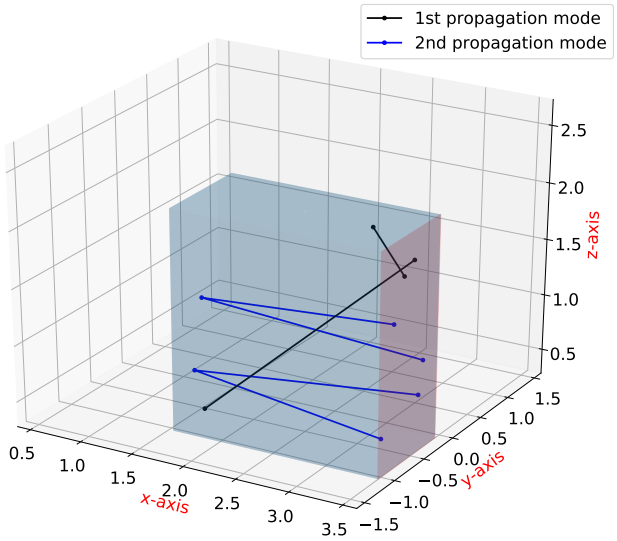


Figure 38: Two modes of propagation of photons inside a BGO crystal with one reflection on the reflector, using LUT model. The red face is the front face of the crystal, the one from which the photons can escape from the crystal. The photon could be reflected on the reflector, and then it goes out (black line), or it could be at first reflected on the front face by internal reflection, then reflected on the reflector, and finally it goes out (blue line). This second mode will be characterized by a longer time, and so the bump observed in Figure 36

## 5. Neutron Detection with OSCAR

In a laser-target interaction, neutrons are produced through nuclear reactions induced by photons, electrons and protons produced in the target, and this radiation contributes to the background signal of electrons and photons. In the current response matrix, neutrons from the target are not included, therefore there is a strong interest in estimating the level of neutrons produced, in order to better evaluate their importance in the experimental background, and eventually add a corrective term in the response matrix.
An order-of-magnitude estimation of the energy of the radiation produced in the target has been performed on the basis of the latest available data from ELIMAIA experiments (the specific target material is not relevant at this stage), and results are reported in Table 3.

| Primary | Energy distribution | Energy | Spatial distribution |
|---|---|---|---|
| Hot electrons | Maxwell-Boltzmann | $\langle kT \rangle = 4$ MeV | Isotropic |
| Cold photons | Maxwell-Boltzmann | $\langle kT \rangle = 40$ keV | Isotropic |
| Hot photons | Maxwell-Boltzmann | $\langle kT \rangle = 4$ MeV | Isotropic |
| Protons | - | 10 - 100 MeV | Forward peaked |

Table 3: Order-of-magnitude estimation of radiation produced at ELIMAIA, on the basis of the latest measurements.

Based on these results, several Monte Carlo simulations have been performed in FLUKA.CERN to estimate the number of neutrons emitted from the target. It has been obtained the yield of neutrons produced from a target 1.0 x 1.0 cm, 100 µm thickness (that is the maximum thickness typically used), made of different materials, i.e. Gold, Nickel, Aluminum, Mylar, and Helium. As a preliminary analysis, only the production of neutrons due to interaction of hot photons and protons with the target itself has been explored. In the simulations, the source of photons has been assumed to be isotropic and placed in the middle of the target itself, while for protons it has been simulated a pencil beam downstream the target with null initial width and divergence of 30 mrad.
The energy spectrum obtained is reported in Figure 39, and it is evident that higher Z targets lead to a larger neutron yield, and that the neutron production due to protons is about 100 times higher than the one due to hot photons.

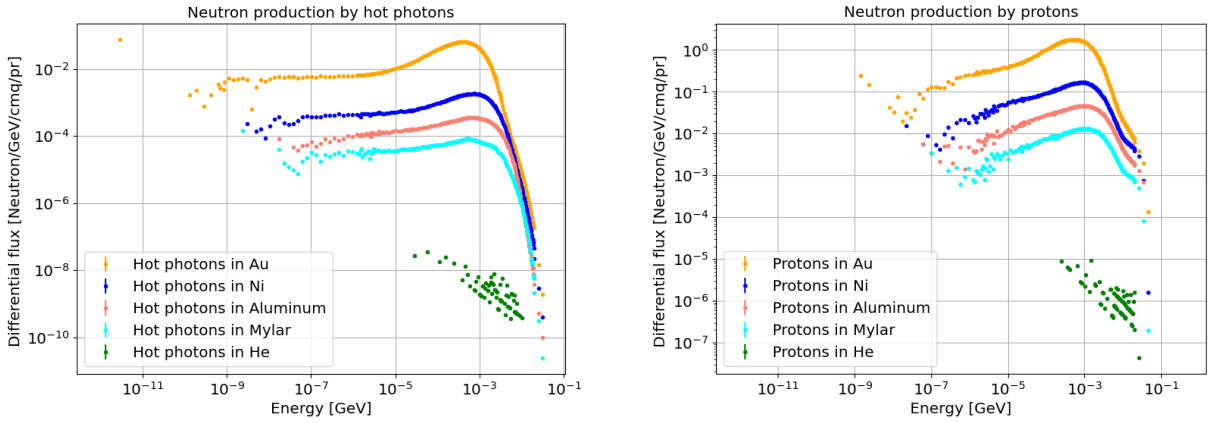


(a) (b)

Figure 39: Differential flux of neutrons produced in target foil 100 µm thick by hot photons (a) and protons (b).

Based on these spectra, the response of OSCAR to neutrons has been compared to the one to electrons and photons for the same temperatures and relative amplitudes used to obtain the neutron yields (from OSCAR's measurements, it is known that hot electrons are 25 times more numerous than hot photons). For simplicity, Birks' effects have been neglected, and this eventually leads to an over-estimation of the signal from neutrons. As shown in Figure 40, the response to hot-photon-induced neutrons is a factor $10^6$ smaller than the one to electrons and photons, and a similar response is expected also for proton-induced neutrons. It should be noticed how PVT scintillators (Crystal ID from 1 to 6) are more sensible to neutrons than BGO crystals (Crystal ID from 7 to 21); this is due to the different mechanism of interaction with the scintillator. In the PVT crystals, neutrons scatter with hydrogen ions, and recoil protons deposit their energy in the crystal, while in BGO crystals the signal mainly comes from the gamma rays produced in inelastic scattering interactions of neutrons with the scintillator [16]. The proven lower sensitivity to neutrons in addition to the small neutron yield (Figure 39) justifies a posteriori having neglected the neutrons produced in the target in the actual response matrix.

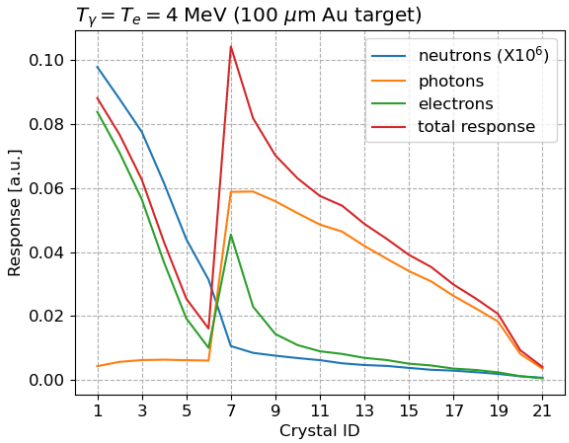


Figure 40: Response matrix for neutrons produced by hot photons ($T_\gamma$ = 4 MeV) in a foil target of gold 100 µm thick compared to response to electrons and photons with $T_\gamma = T_e$ = 4 MeV.

Neutrons could be also seen as the main signal to detect instead of a mere background, and for this purpose OSCAR should be evidently adapted in the design, to significantly improve its capabilities in detecting this type of radiation. For this purpose, it could be interesting to use scintillating crystals with $^6$Li impurities [45]. For discriminating the signal from neutrons to electrons/photons in a neutron-optimized design of OSCAR, there are mainly two possible techniques that could be explored:

- Material discrimination: following the same principle at the basis of the discrimination between electrons and photons, the OSCAR detector could be segmented in various portions with different kinds of scintillators with different neutron sensitivities.

- Temporal discrimination: information related to the type of particle interacting with a scintillating crystals can be obtained observing variations in the signal pulse shape [46], and this is at the basis of the so-called pulse shape discrimination (PSD) method. Although this technique proved to work well with plastic scintillators, it cannot be used with BGO crystals because of the long scintillation time. An additional complication also comes from the electronic readout circuit. In fact, a high bandwidth TIA would be needed as a first stage after the SiPD, and then the signal should be sent to a fast ADC. This has to be done for each crystal, so a 21 channel system has to be adopted, and signals have also to be delayed among them using a sophisticated fiber delay system, making the total calibration of the system quite complex, other than the system itself very expansive.

## 6. Conclusions

The OSCAR calorimeter is a novel concept of active detector specifically designed for online diagnostics and radiation spectrometry for laser-driven experiments conducted at ELI Beamlines. Although the detector has already been largely tested, and its development is quite advanced, several aspects related to light output optimization and readout system limitations deserved a deeper envelopment. Therefore, the use of $TiO_2$ painting as reflector layer has been explored, and the current CMOS camera based readout system has been analyzed in more detail. In particular, the camera background has been measured over long time scales, and results highlighted important variations in time that could affect the quality of the measurements. In addition, point-of-view effects related to the camera have been discussed. An alternative readout system, based on silicon photodiodes, has been also proposed, and a preliminary evaluation of the electronic hardware connected to the photodiode has been reported.
The strong interest in exploring the propagation of the scintillation light inside the crystal pushed the development of two new optical models to be implemented in the FLUKA.CERN code. These optical models have been compared to the basic model available in FLUKA.CERN, and point of view experimental data has been used for benchmarking. The shape of the POV curve obtained from measurements has been reproduced with an error comparable to the experimental one. In addition, the relative light intensities among crystals with different setup (width, material) has been predicted within an error of few percent.
Starting from the newly developed optical models, it has been also possible to analyze the time structure of optical photons propagating in the crystal, and so to predict the time straggling. This could be important to discriminate different type of particles using pulse shape discrimination techniques, expanding the detection capabilities of OSCAR to neutrons.
Finally, the OSCAR's sensitivity to neutrons has been better understood: starting from neutron spectra obtained through simulations, the response of the detector to neutrons has been compared to the one to electrons and photons, showing six order of magnitude lower sensitivity than to the latter. This result confirms that omitting neutrons from the response matrix as ELIMAIA is a valid assumption. Furthermore, this low neutron sensitivity indicates that further development in design and readout techniques are necessary to achieve direct neutron detection with OSCAR, and possible improvements have been proposed.

## References


[1] Eli Beamlines. https://www.eli-beams.eu.

[2] Vojtech Stránský. *Development of Active Diagnostics for Laser-Generated Radiation Using FLUKA*. PhD thesis, Czech Technical University in Prague, 2020.

[3] Tatsufumi Nakamura, James K. Koga, Timur Zh. Esirkepov, Masaki Kando, Georg Korn, and Sergei V. Bulanov. High-power $\gamma$-ray flash generation in ultraintense laser-plasma interactions. *Phys. Rev. Lett.*, 108:195001, May 2012.

[4] C. P. Ridgers, C. S. Brady, R. Duclous, J. G. Kirk, K. Bennett, T. D. Arber, A. P. L. Robinson, and A. R. Bell. Dense electron-positron plasmas and ultraintense gamma rays from laser-irradiated solids. *Physical Review Letters*, 108(16), April 2012.

[5] V. Istokskaia, V. Stránský, L. Giuffrida, R. Versaci, F. Grepl, M. Tryus, A. Velyhan, R. Dudžák, J. Krása, M. Krupka, S. Singh, D. Neely, V. Olšovcová, and D. Margarone. Experimental tests and signal unfolding of a scintillator calorimeter for laser-plasma characterization. *Journal of Instrumentation*, 16(02):T02006–T02006, February 2021.

[6] S. C. Wilks, W. L. Kruer, M. Tabak, and A. B. Langdon. Absorption of ultra-intense laser pulses. *Phys. Rev. Lett.*, 69:1383–1386, Aug 1992.

[7] M Haines, Mingsheng Wei, Farhat Beg, and Richard Stephens. Hot-electron temperature and laser-light absorption in fast ignition. *Physical review letters*, 102:045008, 01 2009.

[8] Matteo Passoni, Luca Bertagna, and Alessandro Zani. Target normal sheath acceleration: theory, comparison with experiments and future perspectives. *New Journal of Physics*, 12(4):045012, apr 2010.

[9] D. R. Rusby, C. M. Brenner, C. Armstrong, L. A. Wilson, R. Clarke, A. Alejo, H. Ahmed, N. M. H. Butler, D. Haddock, A. Higginson, A. McClymont, S. R. Mirfayzi, C. Murphy, M. Notley, P. Oliver, R. Allott, C. Hernandez-Gomez, S. Kar, P. McKenna, and D. Neely. Pulsed x-ray imaging of high-density objects using a ten picosecond high-intensity laser driver. In Keith L. Lewis and Richard C. Hollins, editors, *SPIE Proceedings*. SPIE, October 2016.

[10] Kazuhisa Nakajima, Jianjun Yuan, Liming Chen, and Zhengming Sheng. Laser-driven very high energy electron/photon beam radiation therapy in conjunction with a robotic system. *Applied Sciences*, 5(1):1–20, December 2014.

[11] E. Esarey, C. B. Schroeder, and W. P. Leemans. Physics of laser-driven plasma-based electron accelerators. *Reviews of Modern Physics*, 81(3):1229–1285, August 2009.

[12] Andrea Macchi, Marco Borghesi, and Matteo Passoni. Ion acceleration by superintense laser-plasma interaction. *Reviews of Modern Physics*, 85(2):751–793, May 2013.

[13] J Badziak. Laser-driven ion acceleration: methods, challenges and prospects. *Journal of Physics: Conference Series*, 959:012001, jan 2018.

[14] Hiroyuki Daido, Mamiko Nishiuchi, and Alexander S Pirozhkov. Review of laser-driven ion sources and their applications. *Reports on Progress in Physics*, 75(5):056401, April 2012.

[15] V. Stránský, V. Istokskaia, R. Versaci, L. Giuffrida, A. Cimmino, D. Margarone, and V. Olšovcová. Development, optimization, and calibration of an active electromagnetic calorimeter for pulsed radiation spectrometry. *Journal of Instrumentation*, 16(08):P08060, August 2021.

[16] Glenn F. Knoll. *Radiation detection and measurement / Glenn F. Knoll*. Wiley New York, 2nd ed. edition, 1989.

[17] Alfred Klett and Albrecht Leuschner. A pulsed neutron dose monitor. In *2007 IEEE Nuclear Science Symposium Conference Record*. IEEE, 2007.

[18] Giacomo Paolo Manessi, Marco Silari, Carsten Welsch, Marco Caresana, and Michele Ferrarini. The LUPIN detector: Supporting least intrusive beam monitoring technique through neutron detection. 09 2013.

[19] Daniele Margarone, G. A. Pablo Cirrone, Giacomo Cuttone, Antonio Amico, and Andò. Elimaia: A laser-driven ion accelerator for multidisciplinary applications. *Quantum Beam Science*, 2(2), 2018.

[20] Giuseppe A. P. Cirrone, Giada Petringa, Roberto Catalano, Francesco Schillaci, and Luciano Allegra. Elimed-elimaia: The first open user irradiation beamline for laser-plasma-accelerated ion beams. *Frontiers in Physics*, 8, 2020.

[21] Eljen technologies. https://eljentechnology.com/products/plastic-scintillators/ej-200-ej-204-ej-208-ej-212.

[22] J. Krzywinski, A. Andrejczuk, R. M. Bionta, T. Burian, J. Chalupský, M. Jurek, M. Kirm, V. Nagirnyi, R. Sobierajski, K. Tiedtke, S. Vielhauer, and L. Juha. Saturation of a Ce:$Y_3Al_5O_{12}$ scintillator response to ultra-short pulses of extreme ultraviolet soft x-ray and x-ray laser radiation. *Optical Materials Express*, 7(3):665, February 2017.

[23] John S. Hendricks. A monte carlo code for particle transport. *Los Alamos Science*, (22), 1994.

[24] FLUKA official website. https://fluka.cern.

[25] Battistoni et al. Overview of the FLUKA code. *Annals of Nuclear Energy*, 82:10–18, August 2015.

[26] C. Ahdida, D. Bozzato, and Calzolari et al. New capabilities of the fluka multi-purpose code. *Frontiers in Physics*, 9, 2022.

[27] Martin Janecek. Reflectivity spectra for commonly used reflectors. *IEEE Transactions on Nuclear Science - IEEE TRANS NUCL SCI*, 59:490–497, 06 2012.

[28] S.R. Cherry, Y. Shao, M.P. Tornai, S. Siegel, A.R. Ricci, and M.E. Phelps. Collection of scintillation light from small BGO crystals. *IEEE Transactions on Nuclear Science*, 42(4):1058–1063, August 1995.

[29] Thorlabs. http://https://www.thorlabs.com.

[30] Hamamatsu photonics. https://www.hamamatsu.com.

[31] Saint-Gobain Crystals. http://www.detectors.saint-gobain.com.

[32] Jerald Graeme. *Photodiode Amplifiers: OP AMP Solutions*. McGraw-Hill Professional, New York, NY, December 1995.

[33] Yong-Gang Zhang and Yi Gu. Al(Ga)InP-GaAs photodiodes tailored for specific wavelength range. In *Photodiodes - From Fundamentals to Applications*. InTech, December 2012.

[34] LTspice XVII. https://www.analog.com.

[35] Jerald Graeme. *Photodiode Amplifiers: OP AMP Solutions*. McGraw-Hill, Inc., USA, 1 edition, 1995.

[36] Md Hasan Maruf, Abdulah Korishe, and Sajib Roy. Analysis of analog receiver front end sections for body-coupled communication. 05 2014.

[37] Mihail O. Cernaianu and Marius Gugiu. EMP and debris mitigation challenges in commissioning experiments at 1 PW level in ELI-NP. https://indico.eli-np.ro/event/159/contributions/487/.

[38] Martin Janecek and William W. Moses. Simulating scintillator light collection using measured optical reflectance. *IEEE Transactions on Nuclear Science*, 57(3):964–970, June 2010.

[39] I. Kandarakis, D. Cavouras, D. Nikolopoulos, A. Episkopakis, N. Kalivas, P. Liaparinos, I. Valais, G. Kagadis, K. Kourkoutas, I. Sianoudis, N. Dimitropoulos, C. Nomicos, and G. Panayiotakis. A theoretical model evaluating the angular distribution of luminescence emission in x-ray scintillating screens. *Applied Radiation and Isotopes*, 64(4):508–519, April 2006.

[40] J. D. Jackson. Electrodynamics, classical, April 2003.

[41] Martin Janecek and William Moses. Optical reflectance measurements for commonly used reflectors. *Nuclear Science, IEEE Transactions on*, 55:2432 – 2437, 09 2008.

[42] Victor R. Weidner and Jack J. Hsia. Reflection properties of pressed polytetrafluoroethylene powder. *J. Opt. Soc. Am.*, 71(7):856–861, Jul 1981.

[43] Gerhard M. Haak, Nelson L. Christensen, and Bruce E. Hammer. Experimental studies on the angular distribution of scintillation light from small BGO crystals. *Nuclear Instruments and Methods in Physics Research Section A: Accelerators, Spectrometers, Detectors and Associated Equipment*, 390(1-2):191–197, May 1997.

[44] Martin Janecek and William W. Moses. Measuring light reflectance of BGO crystal surfaces. *IEEE Transactions on Nuclear Science*, 55(5):2443–2449, October 2008.

[45] Nerine J. Cherepy, Robert D. Sanner, Patrick R. Beck, Erik L. Swanberg, Thomas M. Tillotson, Stephen A. Payne, and Charles R. Hurlbut. Bismuth- and lithium-loaded plastic scintillators for gamma and neutron detection. *Nuclear Instruments and Methods in Physics Research Section A: Accelerators, Spectrometers, Detectors and Associated Equipment*, 778:126–132, April 2015.

[46] M.L. Roush, M.A. Wilson, and W.F. Hornyak. Pulse shape discrimination. *Nuclear Instruments and Methods*, 31(1):112–124, December 1964.

# Abstract in lingua italiana

Nell'interazione di un fascio laser ad alta intensità con un materiale bersaglio, una frazione non trascurabile dell'energia viene dissipata sotto forma di radiazione ionizzante, composta principalmente da elettroni e raggi gamma, le cui caratteristiche dipendono fortemente dalle proprietà del plasma che si genera nel target. Essendo tale radiazione pulsata nel tempo, gli strumenti convenzionali per la spettroscopia nucleare non possono essere utilizzati, in quanto si basano sulla misura di singoli quanti di radiazione per interazione. In questo contesto è stato sviluppato OSCAR: un innovativo rivelatore composto da scintillatori che può essere utilizzato per caratterizzare in tempo reale la radiazione prodotta in esperimenti laser-target. Il lavoro di tesi si è incentrato nell'analisi e ottimizzazione della risposta alla radiazione di OSCAR. Si sono analizzate le variazioni nel tempo del rumore della camera CMOS utilizzata nell'attuale sistema di acquisizione della luce di scintillazione, e si è indagato come l'intensità del segnale luminoso vari con la posizione della camera rispetto al materiale scintillante. Tali studi hanno evidenziato alcune problematiche del sistema di acquisizione in uso, e si è quindi proposto l'utilizzo di fotodiodi al silicio in alternativa alla fotocamera CMOS. Si è inoltre esplorato l'uso del $TiO_2$ come materiale riflettente da applicare sui cristalli scintillanti, al fine di massimizzare il segnale luminoso raccolto dal sistema di acquisizione. La propagazione della luce di scintillazione è stata studiata anche attraverso simulazioni Monte Carlo, eseguite con l'utilizzo del codice FLUKA.CERN. Nuovi modelli ottici sono stati appositamente sviluppati e implementati in FLUKA.CERN per includere la riflessione dei fotoni su superfici non lisce. La differenza tra la distribuzione spaziale della luce di scintillazione ottenuta dalle simulazioni e i dati acquisiti è comparabile all'errore sperimentale. È stato inoltre stimato lo sfasamento temporale dovuto alla propagazione dei fotoni all'interno del materiale scintillante, che deve essere considerato nello sviluppo di tecniche di rivelazione basate sulla struttura temporale del segnale luminoso emesso. Infine, si è valutata la capacità di rivelazione dei neutroni di OSCAR. La bassa sensibilità ai neutroni stimata indica la necessità di ulteriori sviluppi sul rivelatore per ottenere la misura diretta dei neutroni, e possibili miglioramenti sono proposti.

**Parole chiave:** Modellazione di rivelatori di radiazione ionizzante, metodi per la diagnostica del plasma, simulazioni ottiche, sistemi di acquisizione della luce di scintillazione.